Lithos 320–321 (2018) 35–48

Contents lists available at ScienceDirect

Lithos

journal homepage: www.elsevier.com/locate/lithos

Rodingitization and carbonation, associated with serpentinization of Triassic ultramafic cumulates and lavas in Othris, Greece

Petros Koutsovitis [a,b,*], Andreas Magganas [b], Theodoros Ntaflos [c], Nikolaos Koukouzas [a]

[a] Centre for Research and Technology, Hellas (CERTH), Egialias 52, Marousi 15125, Attica, Greece
[b] National and Kapodistrian University of Athens, Faculty of Geology and Geoenvironment, Department of Mineralogy and Petrology, Panepistimioupoli Zografou, 15784 Athens, Greece
[c] University of Vienna, Department of Lithospheric Research, Althanstr. 14, Vienna, Austria

ARTICLE INFO

Article history:
Received 20 June 2018
Accepted 23 August 2018
Available online 31 August 2018

Keywords:
Wehrlites
Ultramafic lavas
Rodingites
Hydrogarnet
Triassic

ABSTRACT

The Othris region in Central Greece includes sub-oceanic crustal rocks of Middle-Late Triassic age that have undergone low to moderate degrees of metasomatic/metamorphic alteration processes. Alteration documented in these rocks includes rodingitization, serpentinization and carbonation in cumulate wehrlites, ultramafic lavas, mafic dykes and pillow-lavas. Wehrlites and ultramafic lavas are partially to completely serpentinized during ocean floor metamorphism. They were additionally affected by rodingitization, mostly expressed with formation of hydroandradites and hydrogrossulars, closely associated with the breakdown of primary phases of clinopyroxene and plagioclase. We estimate that rodingitization occurred within relatively mildly oxidizing physicochemical conditions, with an increased CO_2/H_2O ratio.

More significant rodingitization affected mafic doleritic dykes that intrude wehrlites: this alteration occurred in parallel to serpentinization of hosting ultramafics via subsequent circulation of relatively alkaline and hydrous fluids. We have calculated that this occurred under low to moderate P-T conditions (180–320 °C, P ≈ 2–5 kbar). Circulation of Ca-rich fluids at shallower crustal levels was responsible for local carbonation phenomena, mostly affecting ultramafic and mafic pillow lavas.

1. Introduction

A non-ophiolitic Middle-Late Triassic igneous and sedimentary sequence crops out throughout the southern region of Othris Mountains in Central Greece. Similar volcano-sedimentary sequences of Triassic age have been reported in North and Central Greece (Pindos, Koziakas, Vardoussia, Evia, Iti, Kallidromo, Skiathos) as well as South Greece (Attica, Argolis, Tyros, Crete) (Barth and Gluhak, 2009; Capedri et al., 1997; Economou and Paraskevopoulos, 1989; Ferrière, 1982; Magganas et al., 1997; Magganas and Kyriakopoulos, 2005; Pe-Piper, 1998; Pe-Piper and Piper, 2002; Pomonis et al., 2007; Smith et al., 1975; Tsikouras et al., 2008). The majority of these Triassic igneous rocks are pillow lavas with E-MORB subalkaline tholeiitic basalts and some alkaline OIB (Ocean Island Basalts) (Monjoie et al., 2008; Koutsovitis et al., 2012). Apparent subduction related rocks have been identified that include: crustal-level ultramafic rocks; high- and low-Mg basaltic dykes and lava flows; intermediate to felsic calc-alkaline volcanic and pyroclastic rocks (Koutsovitis et al., 2012).

Formation of the Hellenic Triassic igneous sequences and their accompanied deep-water sediments has been attributed to an early to mid-Triassic rift episode of the Gondwana's northeast margin (Pe-Piper and Piper, 2002; Robertson, 2007; Robertson et al., 1991). Thus, the Pelagonian microcontinent was detached from Gondwana (Apulia promontory) forming the Pindos oceanic basin. The Pindos remained open at least until the Late Cretaceous–Paleocene (Ferrière et al., 2016; Robertson, 2004; Koutsovitis 2017). The occurrence of subduction-related rocks of variable composition (ranging from ultramafic to felsic), with clearly rift-associated basalts has been attributed to intra-oceanic local compressional tectonics that caused a breakup of the early formed oceanic crust, resulting in the formation of an infant subduction zone (Koutsovitis et al., 2012).

The Othris Triassic igneous rocks underwent metasomatic and/or metamorphic alteration of variable degrees. These processes include serpentinization, rodingitization and carbonation. The present study focuses on distinguishing and interpreting the percolation of metasomatic fluids and the metamorphic imprint on the Middle-Late Triassic ultramafic and high-Mg mafic rocks, from a mineralogical, petrological, geochemical and geotectonic viewpoint. Herein we present field observations, new petrographic, mineralogical and whole-rock chemistry data from these ultramafic lavas and cumulates.

* Corresponding author at: Centre for Research and Technology, Hellas (CERTH), Egialias 52, Marousi 15125, Attica, Greece.
E-mail address: koutsovitis@certh.gr (P. Koutsovitis).

https://doi.org/10.1016/j.lithos.2018.08.027
0024-4937/

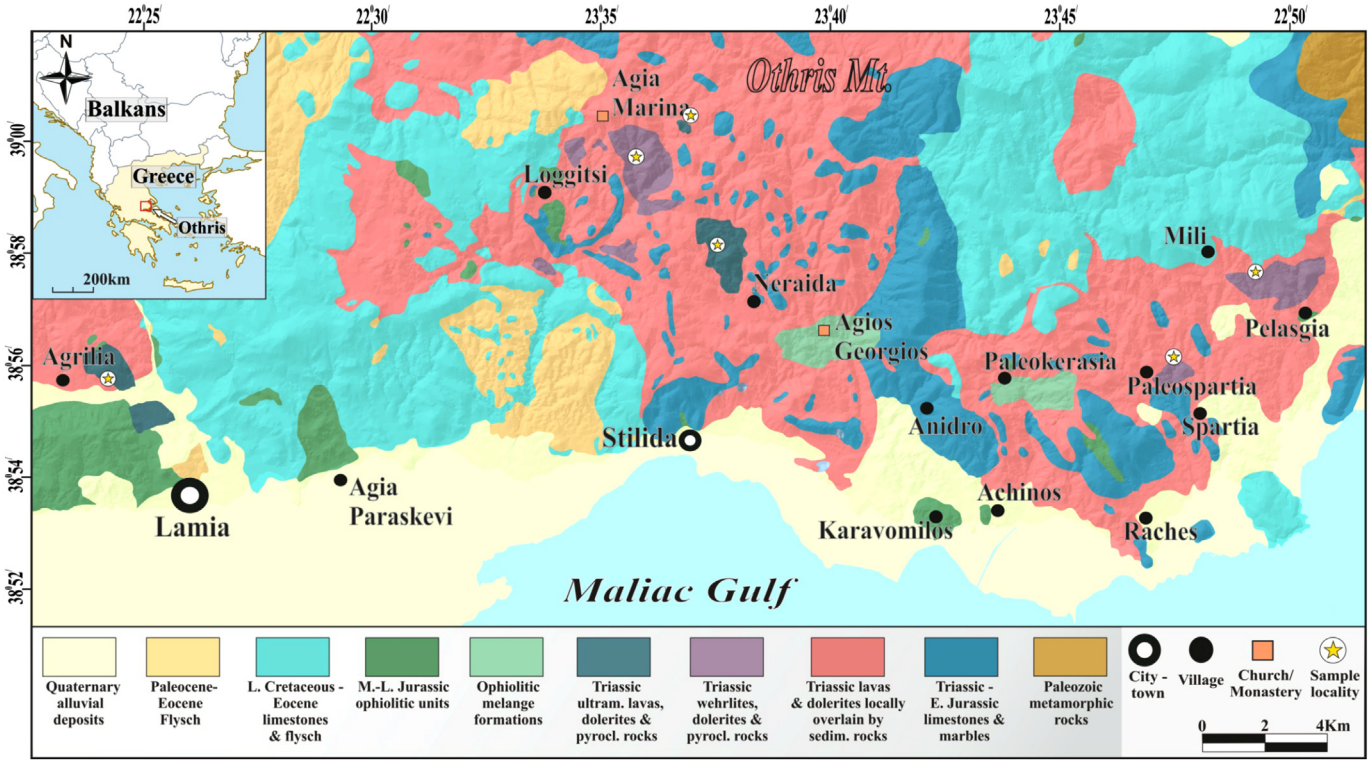

Fig. 1. Geological map of the Eastern Thessaly region (modified Othris map of Koutsovitis, 2009, with additions from the 1:50,000 geological maps of the Othris region of the Greek Institute of Geology and Mineral Exploration).

2. Geological setting

The pre-Alpine crystalline basement of the Othris region (Fig. 1) consists of Late Permian to Early Triassic schists, metapelitic rocks, quartzites, marbles and granitic gneisses (Pe-Piper and Piper, 2002; Smith et al., 1975). It is overlaid by Early to Middle Triassic (Anisian) dolomitic or marly limestones, and these are overlaid by siliceous or brecciated limestones (Ferrière, 1974, 1982; Pe-Piper and Piper, 2002; Price, 1977; Smith et al., 1975). The Middle-Late Triassic igneous and sedimentary sequence of our study is a thick (~250 m) non-ophiolitic unit occurring above the aforementioned carbonates. The sequence outcrops as a series of inverted and imbricated thrust sheets in the south Othris region (Ferrière, 1982; Koutsovitis et al., 2012; Magganas and Koutsovitis, 2015; Smith et al., 1975; Smith and Rassios, 2003). Pillow lavas and lesser lava flows, sub-volcanics and pyroclastic rocks dominate this sequence (Koutsovitis et al., 2012; Smith and Rassios, 2003). These imbricates include thin layers of rhythmically bedded Late Triassic (Early Norian) radiolarian cherts and minor shales (Smith et al., 1975), or are interbedded with Late Triassic (Carnian to Norian) siliceous limestones (Ferrière, 1974). These sedimentary associations imply a stratigraphic age of the volcanic suite of Middle to Late Triassic, and this age has been confirmed by geochronological data: $^{40}Ar/^{39}Ar$ radiogenetic dating of an ultramafic rock sample from the volcanic suite, yielded an age of 243±5 Ma (Roddick et al., 1979).

The tectonically complex Triassic sequence occurs deformed and strato-tectonically beneath Jurassic deep-water sedimentary rocks (pelagic limestones, radiolarites) of the Sub-Pelagonian (or Maliac) tectonostratigraphic zone and Jurassic ophiolites (Dijkstra et al., 2001; Ferrière, 1982; Koutsovitis, 2012; Smith, 1979; Smith et al., 1975; Smith and Rassios, 2003; Spray et al., 1984). The ophiolites were emplaced during closure of the Mesozoic Neotethys in ductile-brittle conditions, initially in the Upper Jurassic – Lower Cretaceous (including initial obduction sole formation) and at a second stage (brittle facies stage) during the post-Paleocene times (e.g. Ferrière et al., 2012, 2016; Papanikolaou, 2009; Robertson, 2002, 2004; Stampfli et al., 2003).

The Othris ophiolites are dismembered and appear in the form of nappes and imbricated thrust sheets (Ferrière, 1982; Smith et al., 1975; Smith and Rassios, 2003). Obduction soles occur over rocks of the Pelagonian tectonostratigraphic zone or of the Middle-Late Triassic igneous and sedimentary sequence. Throughout Greece the Jurassic ophiolitic units and their host rocks of the Pelagonian zone are interpreted as remnants of one or more Tethyan ocean basins originally between Laurasia and Gondwana during the Mesozoic-Early Tertiary (Magganas, 2002; Pomonis et al., 2007; Robertson, 2002, 2004; Smith and Rassios, 2003; Stampfli et al., 2003).

The Triassic – Jurassic sections of Othris are all unconformably overlain by Upper Cretaceous, reefal carbonates (medium to thickly layered carbonate and dolomitic sedimentary rocks), which is then overlain by Paleocene to Eocene flysch (Ferrière, 1982; Papanikolaou, 2009). Flysch consists of reddish to grey shales and thin layered mudstones, with inclusions of thin bedded limestones, sandstones and conglomerates (Katsikatsos, 1992; Magganas and Koutsovitis, 2015; Papanikolaou, 2009; Rassios, 1990). Pillow lavas of the Triassic sequence are ellipsoidal-shaped lobes of lava. Despite regional deformation and alteration, many of these appear exceptionally coherent providing modeling of flow-directions within outcrop scale. Pillow interiors display intersertal to interstitial subophitic textures and vitrophyric to glassy chilled margins. Amygdules (up to 5 mm) are filled by secondary calcite or zeolite minerals. Vesicles in some lavas are elongated or tubular in shape due to deformation.

Highly porphyritic massive or layered ultramafic lava flows occur above the pillow lavas in Neraida, Agia Marina and Agrilia (Fig. 1). Ultramafic cumulates occur as igneous bodies intruded into or interstratified within the pillow lavas and are generally medium to coarse grained wehrlites (Koutsovitis et al., 2012). Wehrlites have been located near the villages of Mili, Agia Marina and Paleospartia (Fig. 1). At the Agia Marina locality, they are found above pillow lavas probably due to tectonic emplacement. Boninitic, basaltic and rarely picritic doleritic dykes are found between or crosscutting these ultramafic rocks and pillow lavas. Massive fabric lava flows overlie the pillow lavas. At some

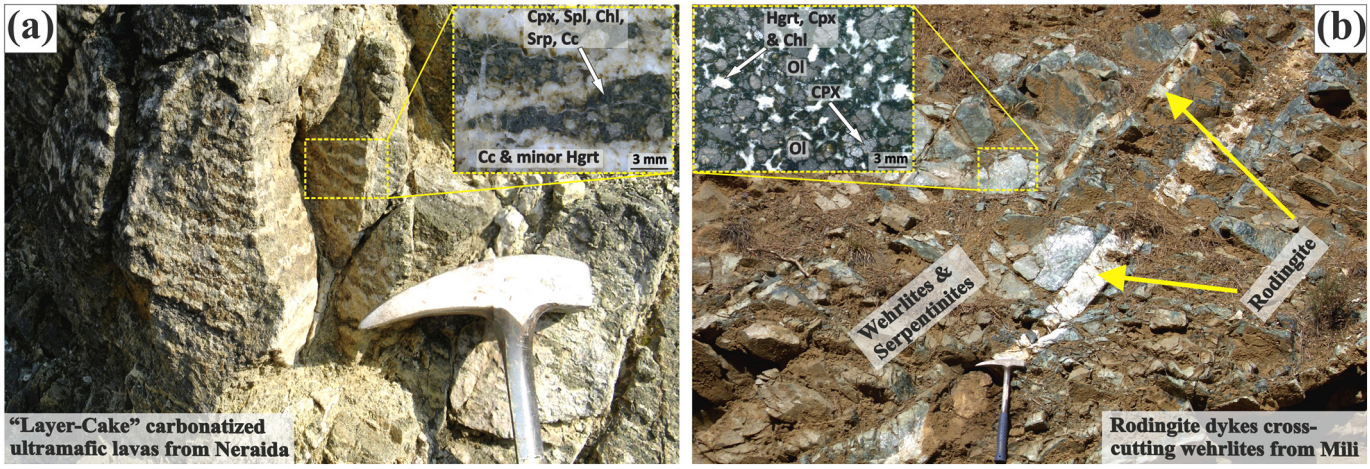

Fig. 2. (a) "Layer-cake" carbonatized ultramafic lavas from the region of Neraida. Enclosed is a stereoscopic image of a polished hand specimen displaying the penetration of calcite. (b) Rodingite dykes crosscutting partially serpentinized and rodingitized wehrlites. Enclosed is a stereoscopic image of a polished hand specimen of a partly rodingitized wehrlite displaying the occurrence of hydrogarnet.

localities, pillow lavas are overlaid by well stratified tuffs of intermediate to felsic composition. The tuffs appear subaqueous; subaerial tuffs may be apparent as welded ignimbrites, but these are rare.

Metasomatism is evident from field observations such as: the occurrence of secondary calcite in pillow lavas and clay minerals at their rims; variable degrees of serpentinization of ultramafic rocks (slight to pervasive); in some localities (Neraida and Agia Marina) extensive carbonation of ultramafic lavas. In the case of carbonation, rocks were intensely penetrated by secondary calcitic-rich veins of variable thickness (0.3-2 cm, rarely up to 4-5 cm) forming remarkable subparallel "layer-cake" infiltrating structures (Fig. 2a). Ultramafic lavas in the Agrilia locality include rare calcite amygdales. Rodingitization affected ultramafic rocks such as wehrlite. The extent of rodingitization varies significantly even amongst samples from the same location. Some of the wehrlite samples were significantly influenced by these processes and hydrogarnet grains can be observed macroscopically. Rodingite dykes up to ~30 cm thick occur with these hydrogarnet-bearing wehrlites (Fig. 2b).

3. Sampling suite and analytical methods

Samples examined in this study include the most representative rocks types of the Triassic igneous group. Ultramafic rocks (including serpentinites), rodingites and dolerites (Table 1) were examined using a Zeiss Axioskop-40 with a Jenoptik ProgRes CF Scan microscope camera at the Laboratories of the Center for Research and Technology, Hellas (CERTH). Table 2 lists major and trace element analyses for five wehrlites, four ultramafic lavas, four serpentinites, two rodingites and four dolerites included in the study. Whole-rock analyses were performed at Bureau Veritas Mineral Laboratories (Acme Analytical Laboratories) in Canada, with the use of ICP-ES for major elements as well as Cr, Ni and ICP-MS for all other trace elements and REE. Detection limits range between 0.01 and 0.04 wt.% for major oxides, 0.01 and 0.1 ppm for trace and rare earth elements. For major and trace element analyses, samples were fused in lithium borate or sodium peroxide, and analyzed for total analysis, whereas structural water was removed from sample powders by heating at 1000 °C for 1 h. Loss on ignition (LOI) was determined from the total weight change, whereas total carbon and sulfur was analyzed by Leco.

Mineral chemistry analyses (Tables S1–S4 in electronic supplementary data) were conducted at the University of Vienna, Department of Lithospheric Sciences using a CAMECA SX-100 electron probe X-ray microanalyzer equipped with five wavelength-dispersive goniometers and one energy-dispersive spectrometer. Operating conditions for minerals were 15 kV accelerating voltage and 20 nA beam current. Beam size was 1 μm for all minerals except for serpentine, chlorite and feldspar with a beam diameter of 5 μm.

4. Results

4.1. Petrography and mineral chemistry

4.1.1. Serpentinized and rodingitized wehrlites

Wehrlites from the regions of Agia Marina and Mili (Figs. 1 and 2b) have been affected by moderate to extensive serpentinization and rodingitization. The original rock fabrics are preserved despite the alteration overprint: minerals are equigranular of medium to coarse grain size with an igneous lamination (cumulate fabric) apparent by the planar orientation of euhedral to subhedral olivine and clinopyroxene grains (Fig. 3a–e). Modal cumulus textured olivine content (15-25 vol. %) varies inversely with the abundance of serpentinite (19-46 vol.%) (Table S1 in supplementary document). Serpentinization affected the rims of residual olivine grains, which is noticed by the lower Fo values of rims compared to cores (Avg. Fo_{cores}~89.8, Avg. Fo_{rims}~87.2). Clinopyroxene (augite or diopside, 15-23 vol.%), and magnesio-hornblende (up to 18 vol.%) seems to be more constant and less dependent upon the extent of serpentinization. Other magmatic-associated minerals include spinel (within olivine, clinopyroxene and serpentine), phlogopite (interstitial crystals or occasionally within clinopyroxene; Fig. 3b, e), magmatic magnesio-hornblende and rare orthopyroxene (small enstatite crystals).

Clinopyroxene grains (augite or diopside following classification of Morimoto, 1988; Table S2 in supplementary document) show a small increase in Ca contents at their rims. Based upon their chemistry, clinopyroxene grains are divided into four types, Type 1a, Type 1b, Type 1c and Type 1d (see Koutsovitis et al., 2012 for more details). Type 1a (cumulus textured) is medium grained, euhedral to subhedral, with their cores presenting considerably high Mg#, moderate to high Wo, as well as highly variable Al_2O_3 and low to moderate TiO_2 contents. The mineral chemistry of Type 1a clinopyroxene rims are highly comparable with their cores, displaying insignificant differences (e.g. slightly higher Wo values). Type 1b clinopyroxene is less frequently present, appearing as small sized subhedral crystals. Compared to Type 1a, they exhibit lower Mg# and Wo values, comparable Al_2O_3 and higher TiO_2 contents. Some clinopyroxene has been affected by metasomatism (single grains or rims of cumulate clinopyroxene). This type of clinopyroxene (Type 1c) has variable Mg# (72.43-91.70), significantly higher Wo (49.20-51.22), variable Al_2O_3 (1.09-5.07 wt.%) and low TiO_2 contents (0.05-0.49 wt.%). Type 1d clinopyroxenes include those that were formed during rodingitization. These are fine grained, mostly

Table 1
Whole-rock major and trace element (ppm) compositions.

Sample	1B/ AMA	3Ol/ AMA	H2/ MIL	H4/ MIL	RU1/MIL	MPSP1/MIL	SP5/ SP	SP6/ SP	PN4/ NER	S1/ MIL
Rock	Wh	Wh	Wh	Wh	Wh	Srp (Wh)	Srp (Wh)	Srp (Wh)	Ul	Ul
Lat.	39°00′ 19″	39°00′ 19″	38°57′ 68″	38°57′ 41″	38°57′ 41″	38°57′ 41″	38°57′ 16″	38°57′ 16″	38°58′ 50″	38°57′ 41″
Long.	22°36′ 54″	22°36′ 54″	22°49′ 81″	22°48′ 39″	22°48′ 39″	22°48′ 39″	22°46′ 17″	22°46′ 17″	22°37′ 39″	22°48′ 39″
SiO_2	43.30	42.67	42.39	42.73	43.38	41.85	41.45	41.39	43.53	45.99
TiO_2	0.44	0.26	0.13	0.16	0.21	0.12	0.10	0.12	0.18	0.24
Al_2O_3	6.03	4.19	4.08	4.05	4.65	2.57	2.20	2.36	3.24	4.81
FeO*	9.11	8.51	8.59	8.45	8.17	7.96	8.26	7.56	7.52	8.64
MnO	0.15	0.14	0.15	0.15	0.14	0.12	0.13	0.12	0.11	0.12
MgO	26.72	29.36	31.09	30.63	29.79	32.68	32.21	33.57	31.01	24.44
CaO	5.46	4.45	3.30	3.47	3.80	1.03	0.70	0.77	2.12	5.53
Na_2O	0.07	0.05	0.07	0.07	0.14	b.d.l	b.d.l	b.d.l	0.04	0.72
K_2O	0.07	0.02	0.04	0.04	0.07	b.d.l	b.d.l	b.d.l	0.05	0.04
P_2O_5	0.06	0.03	0.02	0.02	0.04	0.02	0.02	0.03	0.06	0.04
LOI	8.1	9.8	9.6	9.7	9.1	13.1	14.4	13.5	11.6	9.4
Total	99.52	99.48	99.46	99.47	99.48	99.45	99.46	99.43	99.46	99.57
Sc	17	14	13	14	13	10	9	10	14	17
V	116	78	53	63	73	48	39	48	74	90
Cr	1081	2333	3524	3100	2504	2751	2894	3059	2094	2833
Ni	998	1463	1153	1209	1338	1548	1735	1721	1568	1361
Cu	26.3	38.2	39.2	26.5	36.2	16	16.3	3.4	42.6	13.5
Zn	44	50	45	43	39	39	41	37	41	28
Rb	2.2	1	1.7	2	2.7	0.3	0.2	0.3	2.6	0.3
Sr	30.4	34.5	14.9	17.3	20	10.7	14.5	14.1	19.7	39.6
Y	7.3	4.9	3.4	4.1	5.6	2.2	2.1	2.2	3.8	6
Zr	25.7	15.4	9.1	12.9	15.8	7	6.2	8.1	12.9	17.7
Nb	4.2	1	0.2	0.4	0.4	0.2	0.3	0.2	0.3	0.2
Cs	0.4	0.2	b.d.l	b.d.l	b.d.l	b.d.l	b.d.l	b.d.l	0.7	b.d.l
Ba	13	4	5	6	5	2	2	<1	25	4
Hf	0.7	0.5	0.2	0.3	0.5	0.3	0.2	0.2	0.4	0.5
Ta	0.4	b.d.l	b.d.l	b.d.l	b.d.l	b.d.l	b.d.l	b.d.l	b.d.l	b.d.l
Pb	0.3	1.2	0.5	0.5	0.8	0.1	0.1	0.5	0.5	0.5
Th	0.3	b.d.l	b.d.l	0.2	0.2	b.d.l	b.d.l	b.d.l	0.1	b.d.l
U	0.1	b.d.l	b.d.l	b.d.l	b.d.l	b.d.l	b.d.l	b.d.l	b.d.l	b.d.l
La	3.7	1.6	1.3	1.7	2.1	0.9	0.9	1.2	2.1	1.9
Ce	7.4	3.3	2.4	3.2	4.8	2	1.2	2.2	4.4	4.8
Pr	0.9	0.51	0.33	0.47	0.66	0.28	0.22	0.31	0.61	0.64
Nd	3.8	2.4	1.6	1.9	3	1.3	1.1	1.5	3	3.1
Sm	1.04	0.56	0.32	0.56	0.7	0.2	0.29	0.29	0.83	0.74
Eu	0.38	0.24	0.15	0.19	0.26	0.13	0.11	0.12	0.25	0.31
Gd	1.23	0.84	0.53	0.68	0.93	0.4	0.33	0.43	0.83	0.95
Tb	0.2	0.14	0.09	0.11	0.16	0.06	0.06	0.07	0.12	0.17
Dy	1.26	0.77	0.56	0.73	1.04	0.36	0.3	0.49	0.72	1.03
Ho	0.3	0.19	0.13	0.18	0.21	0.1	0.07	0.1	0.14	0.26
Er	0.85	0.58	0.37	0.46	0.68	0.3	0.25	0.32	0.47	0.64
Tm	0.13	0.08	0.06	0.07	0.09	0.04	0.03	0.04	0.06	0.09
Yb	0.83	0.55	0.36	0.48	0.51	0.25	0.22	0.3	0.36	0.63
Lu	0.12	0.08	0.06	0.07	0.08	0.04	0.04	0.04	0.05	0.1
Mg#	79.64	82.14	82.83	82.86	82.94	84.55	83.87	85.55	84.61	79.04
Tot/C	0.02	0.05	0.05	0.03	0.04	0.04	0.13	0.05	0.04	0.03
Tot/S	0.02	0.03	0.05	0.05	0.04	b.d.l	b.d.l	0.02	0.03	b.d.l

Sample	S2/ MIL	PN1/ NER	PN2/ NER	250/ NER	2C/ AMA	2D/ AMA	2F/ AMA	342/ MIL	R1/ MIL	R2/ MIL
Rock	Ul	Srp (Ul)	Carb.-Ul	Carb.-Ul	Bon	Bon	Bon	Rond	Rond	Rond
Lat.	38°57' 41''	38°58' 50''	38°58' 50''	38°58' 03''	39°00' 19''	39°00' 19''	39°00' 19''	38°57' 41''	38°57' 41''	38°57' 41''
Long.	22°48' 39''	22°37' 39''	22°37' 39''	22°38' 16''	22°36' 54''	22°36' 54''	22°36' 54''	22°48' 39''	22°48' 39''	22°48' 39''
SiO2	44.75	41.49	41.47	24.15	48.42	48.38	50.49	40.55	36.9	35.79
TiO2	0.26	0.12	0.17	0.13	0.73	0.74	0.84	0.79	0.82	0.91
Al2O3	5.15	2.46	3.21	2.26	15.72	16.12	15.86	13.51	13.73	13.91
FeO*	8.04	8.16	7.12	4.73	5.55	5.75	6.57	7.77	5.94	6.06
MnO	0.12	0.14	0.11	0.08	0.09	0.1	0.12	0.18	0.17	0.15
MgO	27.58	33.35	26.28	14.65	9.56	9.25	8.41	16.8	19.65	15.77
CaO	3.36	0.29	6.64	26.72	11.84	11	8.77	14.12	13.04	18.87
Na2O	0.59	0.01	0.07	0.05	2.93	2.89	3.94	0.15	0	0.02
K2O	0.04	0.01	0.07	b.d.l	0.44	0.94	0.73	0.05	0	0
P2O5	0.05	0.02	0.06	0.05	0.09	0.09	0.13	0.12	0.14	0.17
LOI	10	13.4	14.3	26.9	4.4	4.5	3.9	6.56	9.2	8
Total	99.52	99.44	99.5	99.72	99.77	99.76	99.76	100.6	99.59	99.65
Sc	17	10	13	15	38	37	36	39	35	36
V	91	47	74	40	228	227	232	283	299	311
Cr	2689	3052	2053	1663	520	486	198	132	137	157
Ni	1293	1669	1443	1081	133	125	83	73	102	107
Cu	11.5	10.7	24.2	22.6	34.4	47.1	72.4	113.1	13.4	21.1
Zn	31	49	39	41	18	23	44	91	27	21
Rb	0.5	0.2	2.8	0.7	6	11.9	7.4	0.8	b.d.l	b.d.l
Sr	32.1	8.6	383.2	136.9	155.5	186.1	238.3	45.5	11.2	13.6
Y	6.3	2.6	4	3.7	13	12.5	17.8	13.6	20.6	24.7
Zr	17.9	7.6	12.7	8.8	42.8	39.9	61.9	42	66.9	81.2
Nb	0.3	0.08	0.2	1.1	6.1	6.1	8.8	1.5	2.1	2.2
Cs	b.d.l	0.08	0.9	0.5	1.1	2.1	0.4	0.1	b.d.l	b.d.l
Ba	5	0.5	24	11	59	88	109	38.1	3	4
Hf	0.6	0.2	0.3	0.3	1.2	1.1	1.7		1.9	2.4
Ta	b.d.l	b.d.l	b.d.l	0.03	0.5	0.4	0.6	0.8	0.1	0.2
Pb	0.4	0.3	0.5	0.5	0.3	0.3	0.8	0.94	b.d.l	0.2
Th	b.d.l	0.1	0.1	b.d.l	0.7	0.5	0.9	0.5	1.2	1.8
U	b.d.l	b.d.l	0.1	0.1	0.2	0.3	0.3	0.15	0.4	0.5
La	2	1.1	1.8	1.5	5.9	6.2	8.9	4.16	7.4	9.1

Table 1 (*continued*)

Sample	S2/ MIL	PN1/ NER	PN2/ NER	250/ NER	2C/ AMA	2D/ AMA	2F/ AMA	342/ MIL	R1/ MIL	R2/ MIL
Rock	Ul	Srp (Ul)	Carb.-Ul	Carb.-Ul	Bon	Bon	Bon	Rond	Rond	Rond
Lat.	38°57' 41"	38°58' 50"	38°58' 50"	38°58' 03"	39°00' 19"	39°00' 19"	39°00' 19"	38°57' 41"	38°57' 41"	38°57' 41"
Long.	22°48' 39"	22°37' 39"	22°37' 39"	22°38' 16"	22°36' 54"	22°36' 54"	22°36' 54"	22°48' 39"	22°48' 39"	22°48' 39"
Ce	5	2.6	4.3	3.3	12.9	13	19.3	10.97	18.4	21.5
Pr	0.7	0.28	0.62	0.43	1.6	1.58	2.38	1.64	2.58	3.03
Nd	3.2	1.2	3	2.5	7.4	6.2	10.4	8.3	12.3	14.2
Sm	0.76	0.28	0.66	0.54	1.79	1.75	2.64	1.93	3.09	3.49
Eu	0.29	0.11	0.24	0.18	0.67	0.63	0.9	0.76	0.92	1.17
Gd	1.03	0.41	0.87	0.54	2.18	2.12	3.16	2.45	3.53	4.33
Tb	0.18	0.08	0.13	0.09	0.38	0.36	0.52	0.4	0.6	0.71
Dy	1.05	0.45	0.72	0.58	2.4	2.09	3.1	2.36	3.81	4.52
Ho	0.21	0.1	0.14	0.1	0.51	0.5	0.69	0.52	0.79	0.99
Er	0.58	0.33	0.46	0.25	1.51	1.48	2.17	1.53	2.35	2.91
Tm	0.11	0.04	0.06	0.03	0.21	0.2	0.31	0.21	0.37	0.42
Yb	0.64	0.27	0.41	0.32	1.33	1.41	1.81	1.45	2.32	2.67
Lu	0.1	0.04	0.05	0.04	0.21	0.21	0.3	0.22	0.32	0.42
Mg#	82.06	84.49	83.11	84.18	69.67	68.2	63.06	74.25	81.52	77.63
Tot/C	0.03	0.04	0.93	5.32	0.03	0.09	0.04	0.06	b.d.l	0.02
Tot/S	b.d.l	b.d.l	b.d.l	b.d.l	b.d.l	b.d.l	b.d.l	0.03	b.d.l	0.05

Notes: Total iron as FeO*, LOI is loss on ignition. Mg# = 100[Mg/(Mg + Fe2+)]. with $Fe2+ = 0.75Fe^{2+}$*.
Abbreviations: b.d.l.: below detection limit. *Rocks*- Wh. Partly rodingitized/serpentinized Wehrlite; Ul. Partly serpentinized Ultramafic lava; Carb.-Ul. Carbonitized-serpentinized-rodingitized ultramafic lava; Srp: Serpentinite; Bon: Boninite; Rond: Rodingite. *Location*- Mili. MIL; AMA. Agia Marina; SPA. Spartia; NE. Neraida.

anhedral crystals, appearing either along with hydrogarnets or found in the form of symplectite textures with hydrogarnets and chlorite. They exhibit highly variable Mg# (74.33-96.68), variable and high Wo (45.42-50.33), as well as very low Al_2O_3 (0.19-1.00 wt.%) and TiO_2 contents (0.01-0.28 wt.%).

Amphiboles are usually magnesio-hornblende, most often appearing to be of magmatic origin (Koutsovitis et al., 2012), as indicated by their textural features and mineral chemistry (e.g. crystallized within type 1a clinopyroxenes; Table S3 in supplementary document). Amphiboles are also present as small tschermakite crystals or as secondary actinolite or tremolite at the rims of primary clinopyroxene and amphibole, but also in some cases along with hydrogarnet, secondary diopside, phlogopite and chlorite.

Serpentinites formed from werhlite protoliths are common at the Paleospartia locality and Mili region. These consist of serpentine, chlorite and minor clinopyroxene, magnetite, spinel and hydrogarnets: this association implies percolation of rodingite-related fluids within the werhlite (Fig. 3f). Serpentine (Table S4 in supplementary document) is present in the form of either lizardite or antigorite. Olivine has been completely replaced by lizardite that forms mesh and hourglass textures, outlined by antigorite lamellae and magnetite (Fig. 3f). Antigorite is also present in the form of blades. Apart from petrographic observations the occurrence of both serpentine polymorphs has been confirmed from XRD patterns from few samples (not shown here). Lizardite has constant SiO_2 content (39.08-42.51 wt.%) and variable MgO (29.49-38.52 wt.%), Al_2O_3 (1.45-5.69 wt.%) and FeO_t (3.38-9.77 wt.%). Antigorite exhibits a higher SiO_2 content (41.61-44.88 wt.%), lower Al_2O_3 (0.05-1.19 wt.%), slightly higher FeO_t (6.25-12.29 wt.%) and more constant MgO (32.41-36.51 wt.%). These mineral chemistry features mentioned for lizardite and antigorite have been outlined by Fryer (2002) and Schwartz et al. (2013).

Rodingitization processes, concurrent to percolation of metasomatic fluids, create a mineral assemblage including hydrogarnet, secondary clinopyroxene (Type 1d), chlorite, tremolite and minor calcite (Fig. 3b–g). Hydrogarnet is often accompanied by secondary diopside and chlorite, appearing as interstitial anhedral masses between olivine and clinopyroxene grains, with highly variable size and modal composition (Fig. 3g). They are often surrounded by chlorite and/or serpentinite and in some cases enclose spinel and magnetite grains. Based upon the textural properties of the least altered wehrlites, it seems that these metasomatic assemblages were formed mostly at the expense of clinopyroxene but also after former plagioclase. In very few cases, the hydrogarnets have pseudomorphically replaced fine grained spinifex textured clinopyroxenes. Serpentine that was formed after pseudomorphically replacing olivine occasionally includes numerous tiny hydroandradite crystals; these form impressive cloudy structures with shapes that resemble those of the former cumulate olivine grains (Fig. 3h).

Most hydrogarnets appearing in metasomatized and serpentinized wehrlites and serpentinites are hydroandradites (Avg. $Adr_{95.0}Grs_{1.6}Prp_{2.9}Sps_{0.1}Uv_{0.4}$); these are characterized by their low Ti-contents (TiO_2<0.7 wt.%) (Table S5 in supplementary document). Some hydrogarnets include Ti up to 7.5 wt.%, in near association with Ti-magnetite or ilmenite crystals. Several other hydrogarnet phases identified include hydrogrossulars (Avg. $Adr_{20.1}Grs_{76.6}Prp_{2.7}Sps_{0.6}Uv_{0.1}$) and mixed series hydrogarnet phases: the latter range between hydroandradite and hydrogrossular end-members (Avg. $Adr_{35.9}Grs_{49.0}Prp_{13.8}Sps_{0.3}Uv_{0.3}$). Hydroandradite was likely formed at the expense of hydrogrossular under lower temperature conditions, since it has been occasionally observed that hydroandradite surrounds hydrogrossular.

The presence of chlorite is closely associated with rodingitization, appearing along with hydrogarnet and secondary diopside (Type 1d clinopyroxenes) in the formation of interstitial anhedral masses between minerals of magmatic origin. The most common types include the Si-Mg-rich and Fe-poor diabantites, penninites and talc-chlorites. Chlinochlore and pycnochlorite have been identified among accessory phases (Table S6 in supplementary document). Pumpellyite, chlorite and in some cases prehnite and hydrogarnet replace cumulus clinopyroxene grains. The FeO_t content (1.3-3.2 wt.%) of pumpellyite is moderate (Table S7 in supplementary document), suggesting the occurrence of balanced oxygen fugacity conditions during metasomatism. Prehnite in wehrlites (Supplementary Table 8) shows moderate Fe_2O_{3t} and MgO contents (0.46–0.52 and ~0.40 wt.% respectively), suggesting similar oxygen fugacity conditions.

4.1.2. Serpentinized and rodingitized ultramafic lavas

The primary fabric of partially serpentinized ultramafic lavas is porphyritic to hyalophyric with interstitial textures: olivine and clinopyroxene are medium grained, euhedral to subhedral phenocrysts embedded in fine-grained and devitrified groundmass (Fig. 3i, j). Cumulus textured olivine phenocrysts are compositionally similar with those in wehrlites but are smaller size. Grains of clinopyroxene (augite or diopside) are classified into two main types (2a and 2b) (Table S2 in supplementary document). Type 2a clinopyroxenes are euhedral to subhedral, quench, hollow, skeletal or rarely blade shaped (Fig. 3j). Their cores present rather high but variable Mg# (74.15–85.89) (lower than the Type 1a clinopyroxenes of wehrlites), moderate Wo (40.04–45.26), as well as moderate and variable Al_2O_3 (2.11-4.67 wt.%), with rather low TiO_2 contents (0.30–0.61 wt.%). Rims, when in contact with devitrified glass, exhibit lower Mg# values and higher TiO_2 contents

Table 2
Elemental gains (+) and losses (−) % estimated for altered rocks with respect to their protoliths, assuming constant Si for serpentinized ultramafics (gray field), constant Cr for carbonitized ultramafics (purple field) and constant Ti for rodingites (gray field).

Sample pairs	Moderately serp. ultr. lava: PN4/NER. Ultr. lava protolith: 357/NER	Significantly serp. ultr. lava: PN1/NER. Ultr. lava protolith: 357/NER	Moderately carb. ultr. lava: PN2/NER Ultr. lava protolith: 357/NER	Extensively carb. ultr. lava: 250/NER Ultr. lava protolith: 357/NER	Altered wehr.: 3Ol/AMA. Wehr. protolith: 363/AMAR	Moderetely serp. wehr.: MH2/MIL Wehr. protolith: 136/MIL	Significantly serp. wehr.: MPS1/MIL Wehr. protolith: 136/MIL	Rodingite: 342/MIL (prehnite-bearing). Protolith: Boninite EX4/MIL	Rodingite: R1/MIL (H. garnet-rich). Protolith: Boninite EX4/MIL
Major elements									
Si	0.0	0.0	−12.8	−37.3	0.0	0.0	0.0	−10.7	−22.2
Ti	−20.6	−44.5	−31.4	−35.3	−17.0	−29.2	−33.9	0.0	0.0
Al	−24.3	−39.7	−31.4	−40.3	−5.8	−27.7	−53.9	−3.5	−6.0
Fe^t	−10.6	1.7	−22.6	−36.5	−7.2	−7.3	−13.0	14.0	−16.5
Mn	−17.9	9.6	−24.9	−32.6	−10.6	−8.2	−19.4	25.8	24.2
Mg	−4.4	7.8	−25.9	−49.0	−13.6	−0.7	5.7	125.7	152.7
Ca	−50.8	−92.9	41.0	600.4	−9.7	−28.3	−77.3	34.2	18.7
Na	−30.7	−34.6	−11.3	−21.7	53.2	−44.9	−33.0	−94.9	−99.7
K	−16.9	−27.3	−17.6	−84.4	−36.2	−2.0	−23.1	−81.0	−97.1
P	−20.3	−32.2	−31.0	−39.1	−34.6	−21.6	−17.3	−1.8	9.0
Total carbon & LOI									
LOI	29.8	57.2	46.4	239.9	19.2	17.6	62.5	10.8	47.8
Total/C	−21.3	−20.9	817.1	6376.3	−17.0	11.0	12.4	14.4	−11.4
Trace elements									
La	−0.6	−45.4	−22.1	−19.8	3.5	27.4	−10.7	−54.4	−22.8
Ce	−18.6	−49.5	−27.2	−31.0	−17.1	−16.0	−29.1	−37.2	0.1
Pr	−25.1	−63.9	−30.4	−40.4	−12.8	−21.2	−32.3	−34.2	−1.5
Nd	−28.5	−70.0	−34.6	−32.7	−22.4	−17.5	−32.1	−16.7	17.5
Sm	−22.6	−72.6	−43.7	−43.1	−32.1	−47.8	−66.9	−23.9	15.8
Eu	−37.8	−71.3	−45.4	−49.4	−32.4	−13.6	−24.1	−10.1	3.5
Gd	−31.2	−64.4	−34.0	−49.4	−21.1	−18.9	−38.0	−20.8	8.6
Tb	−27.3	−49.1	−27.9	−38.4	−16.2	−32.2	−54.2	−33.5	−5.1
Dy	−22.4	−49.1	−29.0	−29.4	−26.3	−8.6	−40.5	−32.1	4.2
Ho	−20.1	−40.2	−26.9	−35.6	−9.0	−15.1	−33.9	−30.0	1.2
Er	−17.1	−39.0	−25.8	−50.2	−14.6	0.7	−17.3	−35.7	−6.0
Tm	−3.0	−32.2	−11.3	−45.2	−4.2	−16.0	−43.3	−36.2	7.0
Yb	−32.9	−47.2	−30.0	−32.6	−15.1	−11.8	−38.0	−33.5	1.2
Lu	−30.7	−41.9	−36.6	−37.4	−4.2	−2.0	−33.9	−31.2	−4.7
Ba	97.1	−95.9	73.2	−2.0	−64.2	63.3	−33.9	1.4	−92.4
Sr	−57.4	−80.5	659.1	234.8	18.0	−41.4	−57.4	−66.0	−92.0
Y	−12.3	−37.0	−15.5	−3.5	−4.2	−12.3	−42.6	−38.9	−12.0
Sc	−16.2	−37.2	−28.8	1.5	−10.6	−25.1	−41.6	−5.7	−19.5
Zr	−30.5	−57.1	−37.4	−46.4	−26.3	−0.9	−22.8	−23.5	16.0
Cr	11.5	70.4	0.0	0.0	−6.7	−2.9	−23.2	−67.7	−68.1
Ni	−4.7	6.5	−19.7	−25.8	−6.7	−21.0	7.5	38.7	84.4
Rb	−9.9	−92.7	−11.3	−72.6	−49.6	−2.0	−82.5	−83.9	−98.5
Th	−73.8	−72.5	−76.0	−98.1	−52.1	47.0	−0.8	−70.4	−32.5
V	−18.4	−45.7	−25.4	−50.2	−1.7	−30.8	−36.5	−5.6	−5.1
Nb	−75.8	−93.2	−85.2	0.4	−43.7	−21.6	−20.6	−71.5	−62.0
Pb	−58.9	−74.1	−62.4	−53.6	−13.0	22.5	−75.2	−56.5	−96.5
Cs	−38.3	−92.6	−27.4	−50.2	−36.2	−60.8	−50.4	52.0	1.2
Mass gains/losses	−3.01%	1.73%	1.81%	9.56%	−4.24%	−2.03%	−0.79%	3.85%	1.22%
Density gains/losses (by CIPW)	0.31%	2.47%	−1.53%	−8.61%	0.00%	0.00%	1.56%	4.71%	4.04%

compared to cores. Type 2b clinopyroxene grains are very small size (~50–100 μm), occurring within devitrified glass and exhibiting hollow or spinifex quench shapes. The Mg# is very low (51.68–64.91) with highly variable Wo, Al_2O_3 and TiO_2 contents (31.82-50.33, 2.60-13.77 wt.% and 0.82-4.22 wt.% respectively). Devitrified glass is present in relatively high amounts in these samples (~20 vol.%) and consists of chlorite, fine grained quench or spinifex textured secondary clinopyroxene, amphibole (tschermakite) feldspar and accessory rhoenite (Fig. 3i, j). The ultramafic lavas include subordinary amphibole (tschermakite), spinel, orthopyroxene and Fe-Ti oxides (Ti-magnetite and Mg-ilmenite). Serpentine, chlorite and titanite are present as secondary minerals.

Serpentinization has variably affected the ultramafic lavas that now consist of (25-41 vol.%) serpentine. Most serpentine is an alteration of phenocrystic olivine (15-23 vol.%) (Table S1 in supplementary document). Serpentinites that represent extensive serpentinization of ultramafic lavas are found only in the region of Neraida. As in the wehrlite suite, the type of serpentine present in the serpentinized ultramafic lavas is lizardite or antigorite. The chemistry of lizardite in ultramafic lavas is highly similar to that in the werhlite suite: SiO_2 (39.46-42.79 wt.%) and MgO (32.74-36.34 wt.%) contents are very similar, Al_2O_3 (0.45-3.62 wt.%) contents are lower than in wehrlites and FeO_t (5.50-11.23 wt.%) contents tend to be higher (Table S4 in supplementary document). Antigorite in ultramafic lavas, compared with antigorite included in wehrlites, has similar SiO_2 (42.09-45.55 wt.%), Al_2O_3 (0.03-1.61 wt.%) and slightly lower FeO_t (3.47-12.35 wt.%) contents, but is more variable in MgO (28.64-37.37 wt.%). Calcite occurs as a minor phase within serpentinite either as small sized calcite amygdules or as veinlets.

Ultramafic lavas from the Neraida locality have experienced extensive carbonation and lesser serpentinization and rodingitization: these resembling ophicalcites (Figs. 2a, 3k), as defined by Fettes and Desmons (2007). Massive microcrystalline calcite intergrowths are present as well as small sized calcite-filled pseudomorphs replacing primary olivine. Mesh or fibrous textured serpentinite (Fig. 3k) is present in these altered lavas. Alteration veins, in addition to calcite, include chlorite and small-sized hydroandradites ($Avg.Adr_{93.7}Grs_{1.3}Prp_{4.8}Sps_{0.0}Uv_{2.3}$), indicating percolation of rodingite-related fluids (Table S5 in supplementary document). Calcite is also found in the form of thinner veins, often being rooted from the main calcitic veins or as secondary calcite filled vesicles (up to 5mm). Clinopyroxene and spinel appear to have been slightly affected by these metasomatic processes. However, in cases where clinopyroxene relicts are in contact or within the calcite-rich veins, they have been subjected to uralitization, having been mostly replaced by tremolite and/or actinolite. Furthermore, rims of spinel grains display

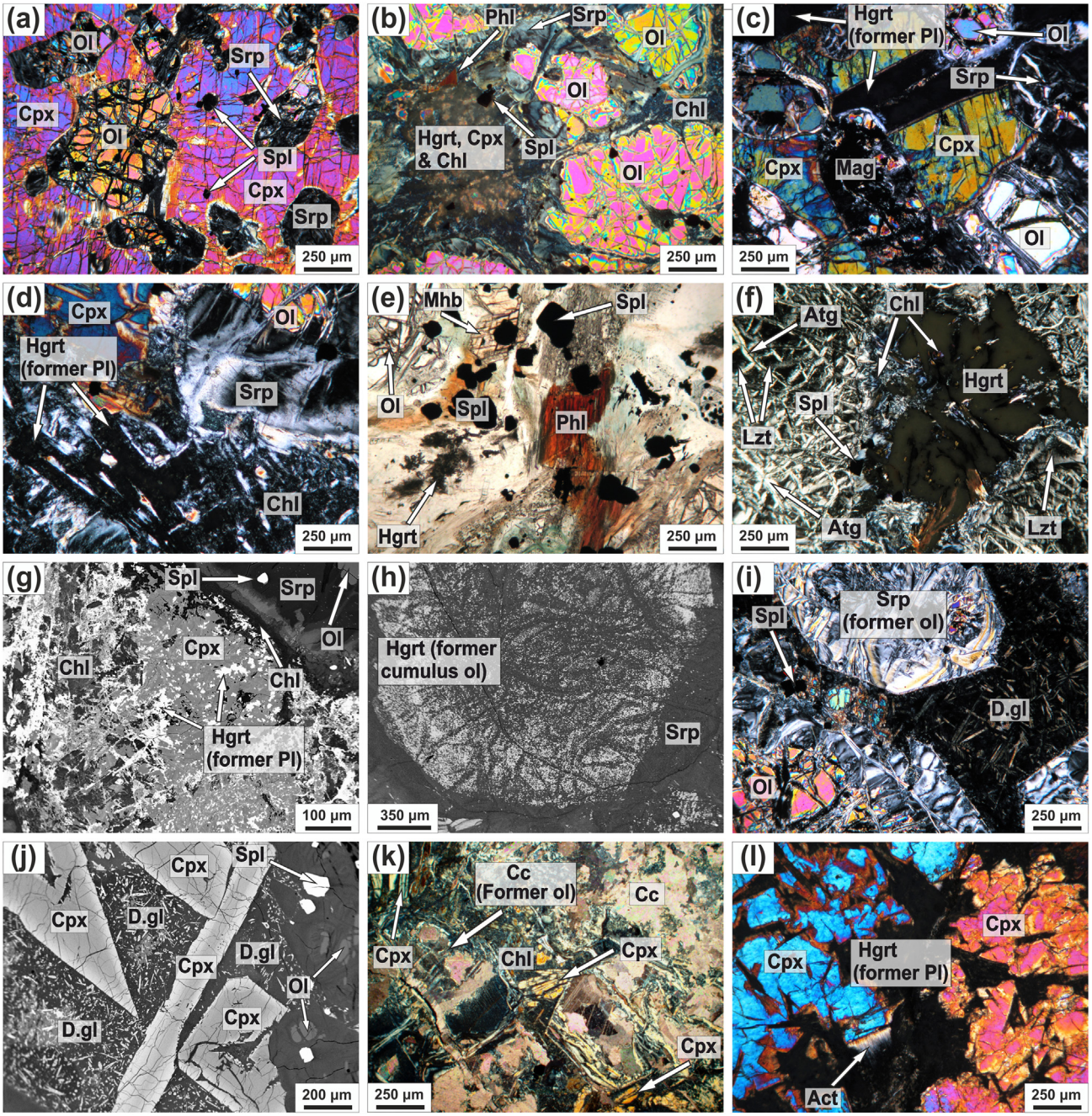

Fig. 3. Photomicrographs and back-scattered electron (BSE) images. (a) (RU1/MIL) Slightly altered wehrlite consisting of partly serpentinized (Serp) cumulus olivine (Ol and spinel (Sp), enclosed by type 1a cumulus clinopyroxene (Cpx). (b) (363/AMA) Metasomatized wehrlite with olivine being partly replaced by serpentine. Hydrogarnet crystals are accompanied by secondary clinopyroxene and chlorite forming interstitial anhedral masses. Accessory phlogopite and spinel also present. (c) (H2/MIL) Metasomatised wehrlite with former plagioclase (Pl) being pseudomorphically replaced by hydrogarnets (Hgrt). (d) (3Ol/AMA) Slightly altered wehrlite with olivine being partly replaced by serpentine and hydrogrossular replacing plagioclase. (e) (RU1/MIL) Phlogopites are frequently present in wehrlites from Mili region. Hydrogarnets and magnesiohornblende also occur. (f) (MPS1/MIL) Serpentinite (former wehrlite), including both serpentine polymorphs (Lzt: Lizardite; Atg: Antigorite), along with hydrogarnet (Hgrt), chlorite (Chl), magnetite and relict spinel. (g) (330/AMA) Metasomatised wehrlite fine-grained aggregates of hydrogarnet, chlorite and secondary clinopyroxene. (f) (MPS1/MIL) Serpentinite in which hydroandradite crystals pseudomorphically replace former olivine. (i) (340/NER) Ultramafic lava consisting of cumulus olivine partly serpentinized, quench clinopyroxene (Cpx) and devitrified glass (D.gl), composed of a matrix of chlorite (Chl) and microlites, along with linear arranged skeletal clinopyroxene (Cpx) and amphibole (Amp) (j) (PN4/NER) Ultramafic lava with relict olivine crystals and devitrified glass (D.gl) composed of a matrix of chlorite (Chl) and microlites, along with linear arranged skeletal clinopyroxene (Cpx) and amphibole (Amp). (k) (250/P. NER) Carbonatized ultramafic lava with linear arranged skeletal clinopyroxene (Cpx) and spinel as the only relict mineral phases. Olivine has been pseudomorphically replaced by calcite, serpentine and minor chlorite. (l) (R1/MIL) Rodingite that mainly consists mainly of hydrogrossular (Hgrs) (former plagioclase) and clinopyroxene (Cpx). Actinolite appears at the rims of clinopyroxene as a result of uralitization.

higher Fe contents and in some cases are surrounded by thin magnetite coronas.

4.1.3. Dolerites and rodingites

Within the Mili region, whitish and greenish coloured rodingitic dykes occur with boninitic or low-Mg basaltic dolerites as intrusions within wehrlites bodies. The boninitic dolerites are comprised of medium to fine-grained plagioclase laths, interstitial clinopyroxene relicts, magnesio-hornblende, devitrified glass and spinel (Table S1 in supplementary document). The doleritic basalts consist of plagioclase and clinopyroxene (forming subophitic textures) and smaller amounts of magnesio-hornblende, devitrified glass and spinel. Secondary mineralization is apparent by the presence of chlorite, fibrous amphibole (mostly actinolite), prehnite, pumpellyite, white mica and titanite.

Rodingites formed after pervasive replacement of the primary minerals of these dolerites. This resulted in a secondary mineral assemblage of: hydrogarnet ± prehnite + clinopyroxene ± amphibole + chlorite ± pumpellyite ± calcite, along with Fe–Ti oxides (magnetite, ilmenite) and titanite (Fig. 3l). Rodingites can be roughly distinguished into those that are hydrogarnets-rich or prehnite-bearing. Hydrogarnet occurs as fine-grained aggregates and rare larger allotriomorphic crystals. Hydrogarnets (Table S5 in supplementary document) are mixed series phase crystals, ranging between hydroandradite and hydrogrossular end-members (Avg. $Adr_{43.2}Grs_{52.3}Prp_{4.3}$ $Sps_{0.1}Uv_{0.1}$ with Ti-contents ranging widely from low to significant amounts (TiO_2=1.1-14.7 wt.%). Hydrogrossulars (Avg. $Adr_{20.0}Grs_{79.2}Prp_{0.6}Sps_{0.1}Uv_{0.1}$) are less common and may also include noticeably high Ti. The occurrence of Fe-enriched pumpellyite is likely attributed to increasing oxygen fugacity conditions. Clinopyroxene in the prehnite-bearing rodingites are of magmatic origin (Table S2 in supplementary document), appearing as subhedral crystals that were subjected to uralitization with concurrent formation of tremolite and/or actinolite along their rims. Clinopyroxene in the hydrogarnet-rich rodingites includes secondary replacive clinopyroxene, either in the form of subhedral or anhedral diopside neoblasts.

4.2. Whole-rock chemistry

On a volatile free basis, moderately altered wehrlites (LOI<9.8 wt.%) show high MgO contents (29.23-35.50 wt.%) and high Mg# values (77.75–82.94), (based upon results of this study -Table 1- and whole-rock chemistry results from Koutsovitis et al., 2012). CaO and Al_2O_3 contents are variable (3.67–7.68 and 4.51–6.60 wt.% respectively), with low alkali contents ($Na_2O + K_2O$ <0.33 wt.%). Cr and Ni contents range from moderate to high (1081-3555 and 998-1429 ppm respectively). Chondrite normalized REE patterns are subparallel (Fig. 4a), with rather enriched LREE (3.5–15.6×CN) [$(La/Yb)_{CN}$=1.3–3.0] and relatively flat MREE and HREE patterns (2.2-7.4×CN and 2.2–5.7×CN respectively). Eu anomalies of most wehrlites are insignificant, although in some cases they vary substantially (Eu_{CN}/Eu^*=0.83-1.24), most likely ascribed to serpentinization, seafloor alteration or to changes of the fO_2 conditions.

Serpentinites that formed from extensive alteration of wehrlite protoliths have higher LOI and MgO contents (13.1-14.4 and 37.85-40.77 wt.% respectively) and higher Mg# values (81.16-85.55) than the moderately altered wehrlites. Compared to the moderately altered wehrlites, the range of CaO and Al_2O_3 is less (0.82-1.19 and 2.59-2.98 wt.% respectively). Serpentinites contain even lower alkali contents ($Na_2O + K_2O$ <0.2 wt.%), whereas Cr and Ni contents are higher (2751-3978 and 1548-1892 ppm respectively). Chondrite normalized REE patterns are subparallel but generally lower than the patterns shown by moderately altered wehrlites (Fig. 4a). LREE in these serpentinites are slightly enriched (2.0–5.1×CN) [$(La/Yb)_{CN}$=2.0-2.8], in comparison to their relatively flat MREE and HREE patterns (1.2-2.7×CN and 1.2–1.9×CN respectively). The ΣREE of the serpentinites have experienced an average decrease of ~53% compared to that of the moderately altered wehrlites.

Moderately altered ultramafic lavas are characterized by variable MgO contents (30.66-35.51 wt.%) and Mg# values (78.91-84.61). CaO and Al_2O_3 contents (2.41-5.17 and 3.69-6.11 wt.% respectively) are slightly lower than those of wehrlites and their alkali contents (Na_2O+K_2O= 0.08-0.70 wt.%) are variable. Cr (1822–2689 ppm) and Ni (1293–1595 ppm) contents compare with those of wehrlites but with a more narrow compositional range. Chondrite normalized REE patterns (Fig. 4b) are subparallel to those of wehrlites, but display higher ΣREE values. Ultramafic lavas have higher LREE (6.4-15.8×CN) [$(La/Yb)_{CN}$=1.7–4.0], but lower MREE (2.9-7.5×CN) and steeper HREE patterns (2.0–4.9×CN respectively). Sample 360/AGR, that has the highest modal percentage of devitrified glass in our study suite, displays the highest LREE values amongst all of the ultramafic samples. Ultramafic lavas have smaller Eu anomalies (Eu_{CN}/Eu^*=0.81–1.15) compared to wehrlites.

Some ultramafic lavas that were affected mostly by carbonation and subsequent serpentinization. These exhibit high CaO contents (up to ~26 wt.%) that are directly linked with the prevailing effects of metasomatism. Cr (1663-2053 ppm) and Ni contents (1081-1443 ppm) in these extensively altered lavas are similar to Cr and Ni contents of less altered ultramafic lavas and thus were not significantly affected by carbonation. REE patterns are lower and subparallel to those of less altered ultramafic lavas (Fig. 4b), with the ΣREE depletion being apparent on an average scale of ~30%. An extensively serpentinized ultramafic sample from Neraida (PN1/NER) shows even greater ΣREE losses (~56%), which are highly comparable to the REE losses documented in serpentinites that replaced wehrlite protoliths.

Doleritic dykes include island-arc tholeiitic (IAT) basalts and boninites (IAT affinities determined by Koutsovitis et al., 2012). These dolerites contain highly variable amounts of MgO (5.96-13.00 wt.%) and Mg# (48.30-64.46). CaO and Al_2O_3 contents (8.57-12.54 and 11.79-17.29 wt.% respectively) and alkali contents (Na_2O+K_2O=3.53-6.63 wt.%), are higher than those of ultramafic rocks in our sampling suite. Cr (143-923 ppm) and Ni (49-155 ppm) contents are significantly lower compared to the ultramafic samples. Chondrite normalized REE patterns of the dolerites (Fig. 4c) are relatively enriched in LREE (13.6-40.9×CN) [$(La/Yb)_{CN}$=1.8-4.2], with steeper MREE and HREE patterns (8.5-25.0×CN and 7.6–15.8×CN respectively). Eu anomalies can be considered as insignificant (Eu_{CN}/Eu^*=0.92-1.03). Rodingites formed from alteration of these basaltic rocks, have significantly higher MgO and CaO contents (17.21-21.74 and 14.43-20.59 wt.% respectively), as well as Mg# values (69.12-77.39) compared to their protoliths. Al_2O_3 contents (14.37-15.19 wt.%) are comparable with those of protoliths basalts, whereas silica contents have been depleted. Cr contents (132-157 ppm) are lower than those of basalts. Ni contents (73-107 ppm) appear slightly enriched.

4.3. Isocon analysis

Major and trace element modifications have been calculated using the isocon method of Grant (1986), a quantified and graphical approach to the mass transfer equation of Gresens (1967). With this method, we compare metasomatized ultramafics, serpentinites and rodingites with carefully chosen protoliths (relatively less metasomatized and serpentinized). Altered rocks and less altered protoliths were sampled in close proximity (a few meters) and display comparable textural and geochemical features. The deviation of mobile elements above and below the isocon line represents the gains or losses during metasomatism in comparison to the protolith.

A moderately altered ultramafic lava (sample 357/NER) has been compared in this method with extensively serpentinized ultramafic lavas and with carbonitized ultramafic lavas (Fig. 5a, b). In this comparison, Si is the least mobile element. For this reason, the isocon lines were drawn assuming silica immobility for both major and trace element isocon plots in preference to trace elements that are generally considered as immobile (e.g. Al, Ti, Zr, Y) but which are highly variable in our sampling suite. The extensively serpentinized ultramafic lavas are depleted in Ti, Al and Ca, features that become more significant in the case of the serpentinite. Na, K, P and most trace elements have been decreased, including elements regarded as being relatively immobile. The degree of clinopyroxene breakdown in these lavas as a result of metamorphism seems to be mainly responsible for controlling the chemical behaviour of these elements. This is also observed for most trace element values, which are decreased with increasing serpentinization, with the exception of Cr, which is enriched.

The only element which seems to remain relatively immobile in the ultramafic lavas even with significant carbonation is Cr and thus the isocon lines were drawn assuming Cr immobility for both major and trace element isocon plots. Carbonitized ultramafic lavas display profound enrichments in Ca, Total/C and LOI, apparently attributed to the presence of calcite. In the case of the calcite-bearing ultramafic sample

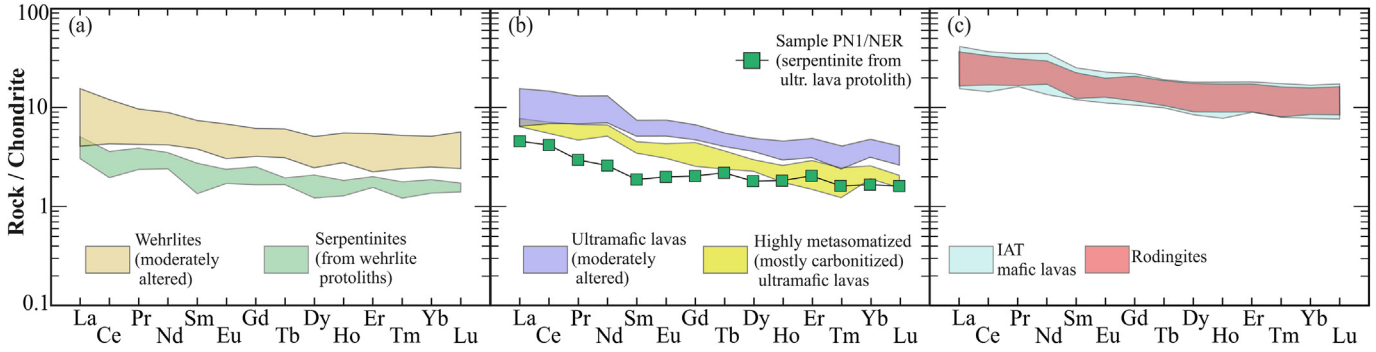

Fig. 4. Chondrite-normalized REE patterns [normalizing factors from Mcdonough and Sun, 1995] of (a) Moderately altered wehrlites and serpentinites, (b) Moderately altered ultramafic lavas and highly metasomatized (carbonitized, serpentinized) ultramafic lavas, (c) island arc tholeiitic mafic lavas (including boninites) and rodingites.

(PN2/NER) it can be observed that most of the other major and trace elements are highly comparable with those of the ultramafic lava protolith (except for Sr). However, with prevailing participation of calcite (sample 250/NER) almost all major and trace element values (except for Ca and Cr) were significantly decreased.

Wehrlites also display silica immobility similar to that documented in the ultramafic lavas. Based on the plots of a sampling pair from Agia Marina (363/MAR-Ol3/MAR) it seems that metasomatism had a rather small effect upon the mobility of most major elements, but was responsible for the restricted depletion of almost all trace elements with the exception of the HREE (Fig. 5c, d). Two sampling pairs from the region of Mili, examines the effects of increasing serpentinization by comparing wehrlites with serpentinized wehrlites and serpentinites (136/MIL-MH2/MIL, 136/MIL-MSP1/MIL respectively). LOI (and degree of serpentinization) is significantly higher in the second pair compared to the first. Most major elements are depleted (except Si and Mg), with this depletion more pronounced in the more extensively serpentinized samples. Trace element contents of the serpentinized wehrlite in these pairs are highly comparable with those of the metasomatized wehrlite. The trace elements of extensively altered serpentinites are relatively low except for the HREE. In contrast to the ultramafic lavas, Cr contents were decreased.

In contrast to the behavior of the ultramafic rocks, rodingites have experienced desilification processes, being more pronounced in the hydrogarnet-rich rodingite. A prehnite-bearing (342/MIL) and a hydrogarnet-rich (R1/MIL) rodingite are compared with a boninite sample (EX4/MIL) from the region of Mili (Fig. 5d, e). Amongst the major elements, Ti and Al remained immobile, similar to variations observed in Jurassic rodingites of Othris (Koutsovitis et al., 2013). This lead us to draw isocon lines assuming Ti immobility for both major and trace element isocon plots. The hydrogarnet-rich rodingite, compared to the prehnite-bearing rodingite, displays slightly higher Ca and Fe and Mn contents and significant Mg and LOI enrichments. Alkali contents are almost completely lost. Trace elements of the prehnite-bearing rodingite have been affected to a higher extent compared to those of the hydrogarnet-rich rodingite, which has maintained its REE.

5. Discussion

5.1. Conditions of metasomatism/metamorphism and element mobility

5.1.1. Serpentinization

All rocks in our study suite include serpentine in variable amounts. Serpentine group minerals identified via petrography and mineral chemistry are lizardite and antigorite; chysotile is present as secondary cross-cutting veins. Lizardite and antigorite replace primary olivine nearly exclusively. The lizardite/antigorite ratios can be regarded as being rather balanced, suggesting serpentinization that took place under moderate temperature and pressure conditions (~320–340 °C, P ≈ 6–7 kbar), that is, within greenschist facies metamorphism (Guillot et al., 2015; Lafay et al., 2013; Schwartz et al., 2013). Antigorite occurrence is attributed to the destabilization of lizardite through the reactions: Lzt → Atg + MgO + H_2O (Vils et al., 2011) or Lzt + SiO_2 → Atg + H_2O (Schwartz et al., 2013).

An increasing extent of serpentinization can be linked directly to an increasing mobility of major and trace elements. Si, Mg and Fe, remained relatively immobile regardless of the degree of serpentinization. We interpret this by the fact that Si and Mg contents amongst olivine and serpentine are highly comparable, whereas Fe was crystallized as small magnetite crystals. Greater values of LOI accompany greater modal contents of serpentine minerals. Decreasing Al, Ca, Ti Na and K contents with increasing serpentinization is attributed to the breakdown of primary clinopyroxene, amphiboles and phlogopite.

Chondrite normalized REE patterns and isocon plots (Fig. 4a, b), show that during serpentinization, trace elements were diluted. HREE generally tend to be more immobile than LREE. Large ion lithophile elements (LILE; Sr, Rb, Cs, Ba) appear to be independent of the degree of serpentinization, which may be interpreted as a result of re-distribution processes (Boschi et al., 2013; Deschamps et al., 2013). The high field strength elements (HFSE), especially Zr and Y, tend to decrease with increasing serpentinization. This may reflect inherited variation within primary clinopyroxene or to the "break-down" of clinopyroxene during serpentinization. The latter may also interpret the significant decrease of ΣREE compared to that of the moderately altered wehrlites. Nickel remains relatively immobile as the serpentine that forms from the alteration of olivine tends to maintain the NiO contents of olivine (Deschamps et al., 2013).

5.1.2. Rodingitization

Two types of rocks were altered via rodingitization processes; ultramafic rocks (wehrlites) and boninite dykes that intrude these wehrlites. Rodingitization of the Othris wehrlites seems a restricted process. In the Mili area, within a cross-section of the sampling locality, successive zones of slightly altered wehrlites occur with hydrogarnet-bearing wehrlites, with rodingite dykes (Fig. 2b) and zones of highly serpentinized wehrlites. A similar phenomenon occurs in the region of Agia Marina wherein the hydrogarnet-bearing wehrlites are found as relatively small occurrences within the main outcrops: these are apparent as small patches within the wehrlites comprised of hydrogarnets (either andradite or grossular-rich), secondary diopside and chlorite.

Petrographic investigation of wehrlites indicates that the breakdown of cumulus clinopyroxene significantly contributed to the formation of hydrogarnets. This breakdown seems to have occurred in two stages; initially clinopyroxene was replaced by pumpellyite and chlorite with minor prehnite, hydrogarnets, tremolite and serpentine (clearly noticed in wehrlite sample 1B/AMA), while at a later stage pumpellyite was replaced by hydrogarnet, chlorite and secondary. Clinopyroxene dissolution as a cause of hydrogarnet formation is evident within

serpentinites that formed post the initial serpentinization of wehrlite protoliths. Serpentine pseudomorphically replaced former cumulus olivine grains. These serpentine pseudomorphs (former olivine) include tiny hydroandradite crystals that develop cloudy structures shaped like the primary olivine grains (Fig. 3h). From these relations, the breakdown of clinopyroxene is associated with diffusive mass transfer of $CaOH^+$ species that participated in the formation of hydrogarnets and secondary diopside, acting as an autometasomatic process during serpentinization. Petrographic examination also documents that the rodingite-related mineral assemblage in wehrlites was also formed at the expense of former accessory plagioclase crystals. In the case of ultramafic lavas they replaced small sized former devitrified glass patches that comprised mostly of chlorite and fine grained quench or spinifex textured clinopyroxene, amphibole and feldspars.

We would like to emphasize that the element mobility behavior observed within Triassic boninites and rodingites of our study suite varies from the values we have measured within Triassic rodingitized ultramafics: Chemical mobilitization within the boninites and rodingites is similar to that previously established in boninites and rodingites that belong to the Jurassic ophiolites of East Othris (Koutsovitis et al., 2013). The East Othris Jurassic rodingites include prehnite-bearing and hydrogarnet-rich rodingite varieties. The predominance of garnet over prehnite is indicative of slightly more extensive desilification processes; boninitic protoliths include feldspar that is almost completely replaced by garnet and/or prehnite, resulting in depletions of silica, but also Na and K (e.g. Bach and Klein, 2009; Frost and Beard, 2007; Schandl and Mittwede, 2001). Apparent Ca enrichment in rodingites can be attributed to the breakdown of primary clinopyroxene of the surrounding wehrlites during serpentinization, concurrent to the diffusive mass transfer of $CaOH^+$ species (e.g. Bach and Klein, 2009; Coleman, 1977; Frost and Beard, 2007; O'Hanley, 1996; O'Hanley et al., 1992; Schandl et al., 1989; Schandl and Mittwede, 2001). The Ti contents remained unaffected during rodingitization, indicating that the circulating fluids were mildly oxidizing (Beard and Hopkinson, 2000; Dubińska, 1997; Knauss et al., 2001). An increase of MgO and LOI is mostly noticed in the hydrogarnet-rich rodingite rather than the prehnite-bearing rodingite, which is assigned to higher chlorite contents.

Regarding the trace elements, we have noted that the Zr and Y contents in the prehnite-bearing rodingite are lower than that of the boninite protolith. These elements are considered as being relatively immobile during metasomatic processes due to the involvement of alkaline fluids (Palandri and Reed, 2004 and references therein). Ni enrichment is most likely due to infiltration of Ni within the rodingites from the concurrent serpentinization of olivine from the surrounding wehrlites. Leaching of Ni is enhanced by mildly oxidizing conditions (Aiuppa et al., 2000; Reimann and De Caritat, 1998). Significant depletions in Cr indicate that it was removed from the protoliths and that infiltration of Cr from the surrounding wehrlites was absent, most likely because spinel grains remained almost unaffected from serpentinization.

Cores from hydrogarnets are enriched in grossular end-member, indicating that the initial rodingitization phase took place under alkaline oxidizing conditions. These hydrogarnets have rims are richer in andradite end-member, probably indicative of increasing fO_2 during the late stages of rodingitization (Barriga and Fyfe, 1983; Dubińska et al., 2004; Li et al., 2004). Similar indications of increasing fO_2 occur in the prehnite-bearing rodingites, since cores of prehnite grains have low Fe_2O_{3t} contents that increase towards their rims. These conditions may have occurred during seawater penetration affecting the rodingitized dykes, and could be consistent with the expected increase of oxidizing conditions when the lithospheric slab was closer to the subducting trench (Kelley and Cottrell, 2009; Rowe et al., 2009).

Chondrite normalized REE patterns and isocon plots (Figs. 4c and 5e, f) indicate that the REE of rodingites (in comparison to their mafic protoliths) were only slightly affected and in some cases almost unaffected by metasomatic processes. The LREE of the prehnite-bearing rodingite seems to be more depleted than that of hydrogarnet-rich rodingite. MREE appears relatively stable in both cases, whereas the HREE experienced limited modifications. The restricted mobilization of the REE is indicative of the prevalence of alkaline fluid phases that allowed preservation of primary clinopyroxene and amphibole, the main REE carriers (Haas et al., 1995; Price et al., 1991; Verma, 1992; Wood, 1991).

Chlorites provide important information regarding the metasomatic history of the rocks included in this study because their composition is sensitive to their temperature conditions of formation. Chlorite geothermometry calculations chlorite geothermometry results (under the calibrations of Inoue et al., 2009; Bourdelle et al., 2013; Lanari et al., 2014; Bourdelle and Cathelineau, 2015), we have found that the chlorites that crystallized along with hydrogarnets in wehrlites were formed under a wide temperature spectrum ranging from 188 to 364 °C, providing evidence that this was a multistage metasomatic process occurring during temperature decrease. The calculated temperatures from chlorites in our rodingite samples are just slightly lower (179-317 °C), and are consistent with those usually estimated for rodingitization processes (~200-340 °C, P ≈ 2-5 kbar; see Palandri and Reed, 2004). Serpentinization also began at temperatures estimated at ~340 °C. It is highly likely that both serpentinization and rodingitization co-occurred during the initial metasomatic stage (Li et al., 2017).

5.1.3. Carbonation

Carbonation processes are known to be closely associated with oceanic hydrothermal activity (e.g. Bernoulli et al., 2003; Kelley et al., 2007; Schwarzenbach et al., 2013; Denny et al., 2015). They occur when circulating Ca-rich alkaline fluids mix with cold seawater becoming capable of forming calcite under relatively lower temperatures compared to temperatures of fluids associated with serpentinization and rodingitization. Carbonitized ultramafic lava outcrops at the region of Neraida, characterized by the formation of "layer-cake" penetrative calcite structures. To form these structures requires continuous Ca-rich fluid percolation infiltrating serpentinized ultramafic rocks. This carbonation process is documented as part of a metasomatic environment, with the presence of small-sized accessory hydroandradites within the calcite matrix.

Based upon the whole-rock chemistry data, carbonation processes appear to have been responsible for changes in the element chemistry of the altered ultramafic lavas. Enrichments in Ca, Total/C and LOI are attributed to the presence of calcite. The variable enrichment of Sr can be assigned to fluid circulation and seawater mixing. The isocon plots (Fig. 5a, b) indicate that the degree of carbonation played an important role in the extent of element mobility. To whit: restricted carbonation allowed most of the major and trace elements to remain almost unaffected, since primary clinopyroxenes with high partition coefficients, remained unaffected. Extensive carbonation with prevalence of calcite resulted in significant element mobility.

5.1.4. Changes in mass and volume

Isocon plots provide information regarding changes in the total mass and volume as a result of metasomatism and low-grade metamorphism. Using the "reciprocal slope" methodology of Grant (1986), the total mass change for our sampling suite is as follows: carbonitized ultramafic lava is calculated at 1.8% (density change -1.5%); serpentinized ultramafic lavas total mass changes vary from -3.0% to 1.7% (density changes 0.3% to 3.1%); metasomatized and serpentinized wehrlites from -4.2% to -0.8% (density changes -0.3% to 1.4%); and rodingites from 1.2% to 3.8% (density changes 4.0% to 4.7%) (see Table 2). Based upon these results, we observe that the total volume tends to increase with carbonation and seems to decrease with rodingitization and serpentinization.

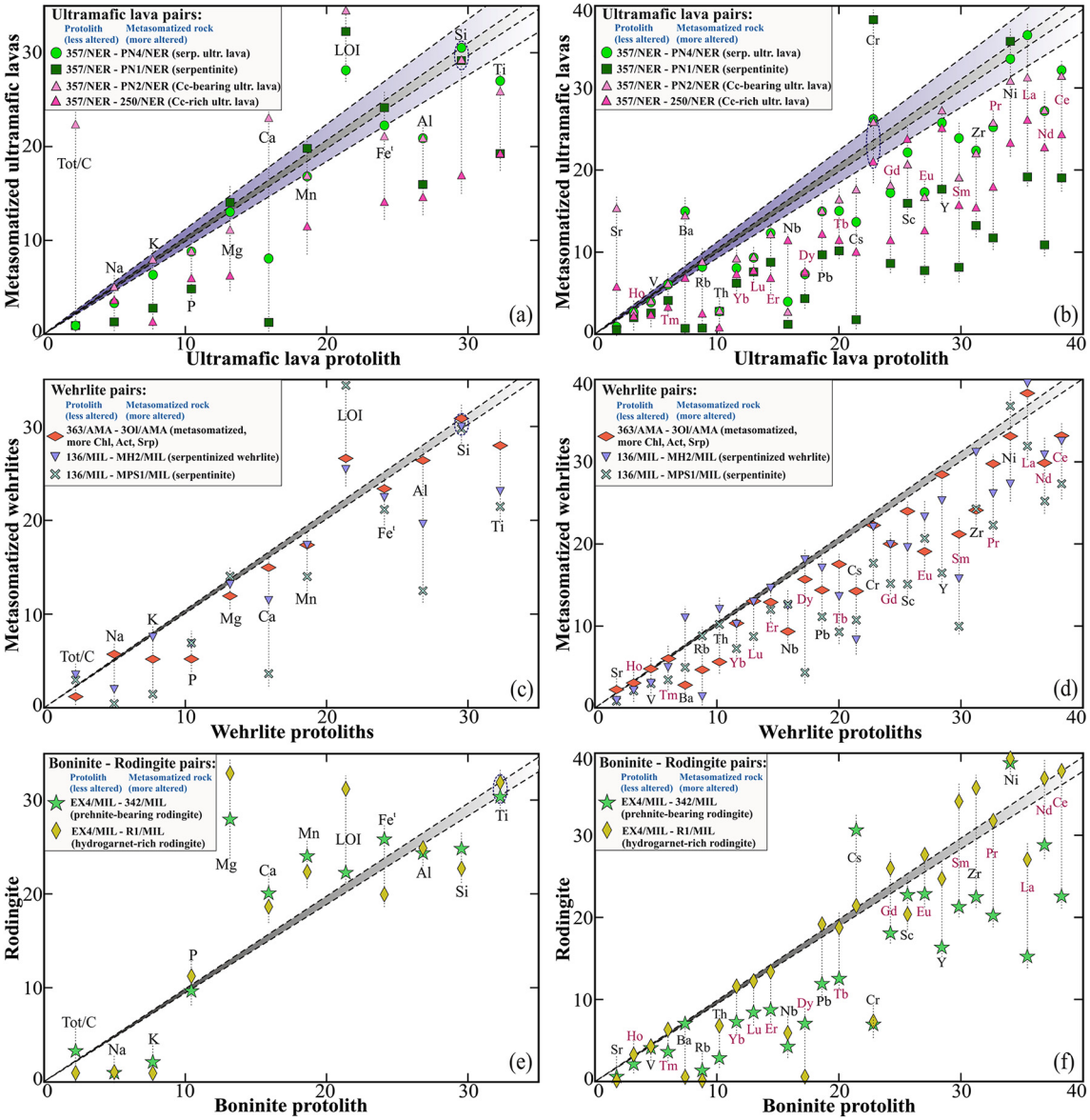

Fig. 5. Isocon plots using the method of Grant (1986) for major elements plotted as wt.% of oxides [(a), (c), (e)] and for trace elements in ppm [(b), (d), (f)]. The grey coloured fields defined by the dotted lines represent constant Si for ultramafics [(a), (b), (c), (d)] and constant Ti for boninite/rodingite pairs [(e), (f)]. Purple coloured fields represent constant Cr for carbonitized ultramafics [(a), (b)]. Scaling factors for ultramafic lavas, wehrlite and boninite/rodingite pairs respectively are: SiO_2 (0.7, 0.7, 0.7, 0.6), TiO_2 (146.8, 107.6, 179.4, 38.9), Al_2O_3 (6.5, 6.3, 4.9, 1.8), FeO_t (3.0, 2.7, 2.7, 3.3), MnO (143.3, 124.2, 116.4, 169.4), MgO (0.4, 0.4, 0.4, 1.7), CaO (3.8, 3.4, 3.5, 1.4), Na_2O (71.0, 497.2, 31.1, 1.6), K_2O (110.1, 256.8, 192.6, 27.5), P2O5 (115.9, 173.9, 347.8, 80.3), LOI (2.5, 2.7, 2.7, 3.4), TOT/C (24.9, 24.9, 74.7, 56.0), Ba (0.6, 0.7, 2.5, 0.2), Sr (0.04, 0.1, 0.1, 0.01), Y (6.8, 5.8, 7.5, 1.2), Sc (1.6, 1.7, 1.5, 0.6), Zr (1.7, 1.6, 3.5, 0.5), Cr (0.01, 0.01, 0.01, 0.1), Ni (0.02, 0.02, 0.02, 0.6), Rb (3.1, 4.6, 5.2, 1.7), Th (27.6, 51.0, 102.1, 5.7), V (0.1, 0.1, 0.1, 0.01), Nb (13.2, 9.3, 63.3, 2.8), Pb (14.6, 13.0, 43.0, 7.5), Cs (19.5, 71.4, 107.1, 306.1), La (17.3, 24.0, 35.4, 3.7), Ce (7.3, 10.0, 13.7, 2.1), Pr (41.3, 58.3, 79.6, 12.3), Nd (7.3, 10.1, 15.7, 2.8), Sm (35.4, 46.6, 61.4, 13.6), Eu (69.3, 79.5, 159.0, 30.0), Gd (20.7, 23.8, 37.9, 7.4), Tb (125.1, 125.1, 154.0, 31.3), Dy (20.7, 18.6, 31.0, 5.0), Ho (18.8, 16.0, 21.3, 4.0), Er (26.2, 22.2, 40.0, 5.7), Tm (100.0, 75.0, 85.7, 17.1), Yb (22.3, 18.7, 29.0, 5.0), Lu (185.9, 162.6, 216.8, 38.3).

5.2. Mineral assemblage evolution and rodingitization reactions

In the ultramafic rocks of this study, the formation of hydrogarnet concurrent to secondary clinopyroxene and chlorite confirms that these rocks were affected by rodingitization processes. This mineralogical assemblage is visible in field and petrographic samples in the form of mineralized patches, mostly in wehrlites and only rarely and less prominent in ultramafic lavas. Petrography and mineral chemistries (see Chapter 4.1) demonstrate that hydrogarnet occurs in wehrlites, mostly appearing as hydroandradite and less often as hydrogrossular or as hydrogarnets with almost equal andradite and grossular end-member values.

Formation of hydrogarnet can be interpreted through reaction (1):

$$Pl + Cpx + H_2O \rightarrow (Hgrs-Hadr) + Chl + Di \pm Cm \quad (1)$$

where Cm symbolizes mobile components that are most often Ca, Na and Si (Li et al., 2008). This reaction is not isochemical and not formulated rigorously. Therefore, either one of the three types of hydrogarnets may form even within the same wehrlite sample.

Reaction (1) alone cannot interpret the occurrence of minerals related with rodingitization of wehrlites. This is because plagioclase, although present, was not a major component in the wehrlite protoliths, and thus was not responsible for contributing to the high amounts of hydrogarnet noticed in some of the samples. Detailed petrography reveals that the breakdown of the cumulus clinopyroxene

significantly contributed to the rodingitization reactions, occurring in two stages.

The first stage includes the mineral assemblage pumpellyite + hydrogarnet + chlorite ± prehnite ± amphibole with relict clinopyroxene, whereas the second stage consists of formation of hydrogarnet + chlorite + diopside (Type 1d) with more abundant hydrogarnet. By applying the software winTWQ 2.3 (Berman, 2007) the following reaction is capable of interpreting the breakdown of cumulus clinopyroxene to pumpellyite and chlorite, under moderate to high CO_2 conditions (Fig. 6):

$$7Cpx + Amph + 5H_2O \rightarrow 4Pump + Chl + CaO_{(aq)} \quad (2)$$

With continuously decreasing temperature conditions and further influx of CO_2, the second stage of rodingitization can be described with reactions (3-5):

$$4Pump + 15Cpx + H_2O + CaO_{(aq)} \rightarrow 6Grt + 3Amph \quad (3)$$

$$20Pump + 15Cpx + 2H_2O + 26CaO_{(aq)} \rightarrow 27Grt + 3Chl \quad (4)$$

$$2Pump + Amph + 2H_2O \rightarrow 2Grt + Chl + Qz \quad (5)$$

The pressure condition for modeling these reactions was set at 4 kbar, since rodingitization usually occurs under low pressures within the range of 0.25-6 kbar and rarely up to 9 kbar (~30 km) (Li et al., 2007; Normand and Williams-Jones, 2007; O'Hanley et al., 1992). The source of highly rich CO_2 fluid solutions is likely interpreted through the transportation of fluids liberated from metamorphic decarbonation of subducted marine sediments and/or mafic rocks (Kerrick and Connolly, 1998; Tsikouras et al., 2009), becoming more significant at depths beneath arcs and affecting mantle-forming rocks (Collins et al., 2015; Cook-Kollars et al., 2014; Piccoli et al., 2016).

Reactions (3) and (4) may also allow us to interpret the absence of desilification processes. These have been observed only in the case of rodingites that formed as a replacement of mafic basaltic dykes. Hydroandradite may have also been formed after replacing hydrogrossular according to the following reaction (6):

$$Hgrs + Cpx + H_2O \pm Cm \rightarrow Hadr + Chl \quad (6)$$

We note that reaction (6) may only interpret the formation of accessory late-stage hydroandradite, with the specific compositional criteria mentioned by Li et al. (2008) (e.g. relatively low FeO and TiO_2, relatively high Al_2O_3 and MnO contents).

We interpret reaction (1) as capable of explaining the mineral assemblages of the rodingites in our sampling suite, as well as explain our observations of desilification processes. The occurrence of prehnite-bearing rodingites may be attributed to the replacement of garnet by prehnite during the last stages of rodingitization (see Koutsovitis et al., 2013). Application of the winTWQ 2.3 software can model reaction (1) under decreasing temperature and CO_2/H_2O ratio conditions, as follows:

$$6Pl + 5Cpx + 4H_2O + 4CaO_{(aq)} \rightarrow 5Grt + Chl + 4Qz \quad (7)$$

Desilification can be attributed to the circulation of low silica fluids derived from the serpentinized ultramafics that host the rodingites (Bach and Klein, 2009; Frost and Beard, 2007; Li et al., 2008). Formation of hydrogarnet at the expense of garnet may have further promoted desilification (Bach and Klein, 2009; Frost and Beard, 2007; Li et al., 2004, 2008) and can be described with the reaction:

$$Grs + 2xH_2O \rightarrow Hgrs + xSiO_2(aq) - fluid \quad (8)$$

Hydrogarnets with balanced andradite and grossular end-members appear as crosscutting veins and veinlets, often accompanied by chlorite and small sized grains of secondary diopside. This suggests that the hydrogarnets formed as a later-stage phase. Ti-bearing hydrogarnet formed during the early rodingitization processes, whereas Ti-rich hydrogarnets developed with consumption of ilmenite, where only few thin lines of relict ilmenite have been retained within the euhedral Ti-rich hydrogarnets. Similar cases have also been noticed in rodingites from other studies (Buse et al., 2010; Koutsovitis et al., 2013 and references therein).

Carbonation processes in the ultramafic lavas of Neraida region were responsible for a significant degree of calcite crystallization, which can be described through reaction (9):

$$Ca^{2+} + HCO_3^- + OH \rightarrow CaCO_3 + H_2O \quad (9)$$

According to Palindri and Reed (2004), this reaction interprets calcite formation from the infiltration of Ca-rich fluids as a result of mixed cold marine seawater and alkaline hydrothermal fluids, associated with the cooling phases of serpentinization.

5.3. Evolution of the oceanic basin

The Triassic ultramafic and high-Mg mafic rocks outcrop as part of an igneous and sedimentary sequence that comprises E-MORB tholeiitic and OIB alkaline basalts. These bimodal basalts point to asthenospheric - plume related volcanic activity in a rifting - extensional regime, which places the Othris suite at the NE part of Gondwana in the Triassic (Koutsovitis et al., 2012; Pe-Piper and Piper, 2002; Stampfli et al., 2003). Based upon mineral chemistry, whole-rock and isotopic geochemical results, the high-Mg ultramafic and boninitic rocks are clearly associated with subduction-related processes (Koutsovitis et al., 2012). We assumed our rock suite to have been formed in the fore-arc setting of an infant, intraoceanic and short-lived subduction zone. Parts of the Triassic volcanic and sedimentary sequence were exhumed as thrust sheets at the accretionary prism due to convergence, whereas other parts of the ocean floor were available for subduction during more recent geological times.

Within this geological context, it is evident that the Othris Triassic igneous rocks underwent mixed conditions of concurrent metamorphic, metasomatic/hydrothermal and tectonic processes. Carbonation affected the shallower rocks (basaltic pillow and ultramafic lavas), caused by hydrothermal leaching and crystallization of calcite within pores and fractures as a result of "hot" carbonated seawater circulation during concurrent serpentinization. Serpentinization affected all of the ultramafic rocks and in some cases (e.g. Spartia region) appears to have formed under greenschist facies conditions. Rodingitization affected both ultramafic (including serpentinites) and high-Mg mafic rocks resulting in the development of hydrogarnet, chlorite, secondary diopside and also of prehnite. This metasomatic process most likely took place during exhumation, under gradually decreasing P-T conditions, either as an autometasomatic process in the case of the ultramafics (closely associated with serpentinization) or with infiltration of fluids within boninitic dykes, associated with serpentinization of the ultramafic neighbouring rocks.

6. Conclusions

Metasomatic and metamorphic processes have affected primary cumulate wehrlites, ultramafic lavas, and associated mafic dykes and pillow-lavas that outcrop within a Middle-Late Triassic igneous and sedimentary sequence in Othris, Central Greece. Ultramafic rocks (wehrlites and ultramafic lavas) are serpentinized in processes that are restricted (moderate alteration) or pervasive, forming serpentinites. Balanced lizardite/antigorite ratios suggest that serpentinization took place under conditions that reached greenschist facies. Most trace element concentrations were relatively decreased during serpentinization. Local rodingitization is characterized by the formation of hydrogarnets,

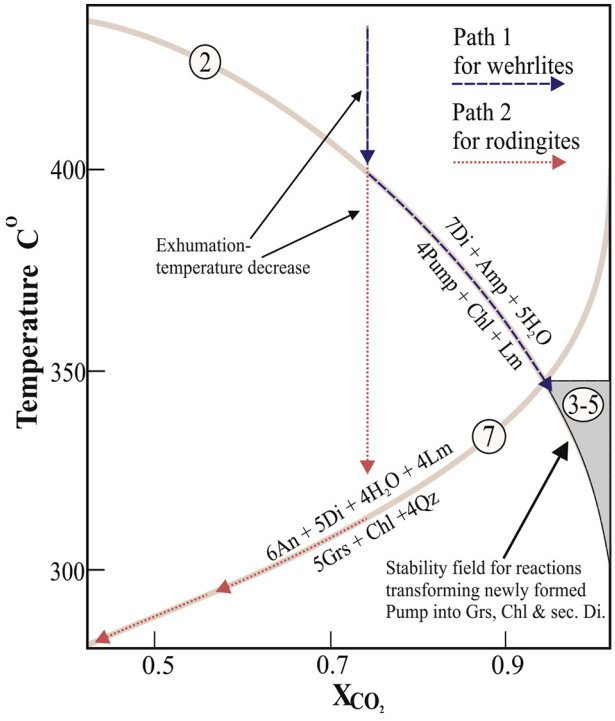

Fig. 6. T–XCO_2 diagram with possible paths interpreting rodingitization phenomena in wehrlites as well as formation of rodingites from mafic protoliths; Abbreviations: An: anorthite, Qz: quartz, Amp: amphibole, Grs: grossular, Di: diopside, Pump: pumpellyite, Chl: chlorite, Lm: lime.

secondary diopside, chlorite, pumpellyite and prehnite. This metasomatic mineral assemblage replaced cumulus clinopyroxene as well as primary accessory plagioclase. Rodingitization occurred with diffusive mass transfer of $CaOH^+$ species under relatively mildly oxidizing physicochemical conditions, along with fluid solutions with an increased CO_2/H_2O ratio.

Rodingites formed as a result of extensive metasomatism that replaced protolithic boninitic dykes intruding wehrlites. The metasomatic hydrous fluids responsible for this process were relatively alkaline, occurring under low to moderate P-T conditions (180-320 °C, P ≈ 2-5 kbar), in conditions of increased fO_2. Rodingites experienced desilification, and rodingitization also resulted in variable decreases and less often increases in trace element concentration.

Carbonation processes affected ultramafic lavas; the most intense carbonation is exposed in the Neraida locality where it has created "layer-cake" structures within the lavas.Metasomatic carbonation was caused by shallow-level continuous circulation of Ca-rich fluids too low in temperature to significantly affect clinopyroxenes. The restricted occurrence of serpentine and hydroandradite indicates that carbonation occurred in association with low-grade serpentinization and rodingitization processes.

The metasomatic phenomena documented herein are related to subduction settings and more specifically to the seafloor exhumation of the mafic–ultramafic rocks in the fore-arc area. We have calculated that serpentinization and rodingitization of wehrlites began within relatively moderate temperature and pressure conditions (~350 °C, P ≈ 6 kbar), with rodingitization processes in both wehrlites and rodingites progressing during further continuous cooling of circulating hydrothermal fluids at shallower depths. The final metasomatic stage is represented by carbonation processes.

Acknowledgments

We would like to express our sincerest thanks to reviewers Dr. Xu Ping Li and Dr. Annie Rassios, and to Editor Dr. Nelson Eby for their constructive reviews, suggestions and critical comments, which significantly helped to improve this paper. Franz Kiraly (ETECH) (University of Vienna) is gratefully acknowledged for assisting with the use of electron microprobe facility. Many thanks are also given to Christos Karkalis (MSc Geologist) for participating in the field and lab work activities, and to Pavlos Krassakis (MSc Geologist) for assisting in the geological map development.

Appendix A. Supplementary data

Supplementary data to this article can be found online at https://doi.org/10.1016/j.lithos.2018.08.027.

References

Aiuppa, A., Allard, P., D'Alessandro, W., Michel, A., Parello, F., Treuil, M., Valenza, M., 2000. Mobility and fluxes of major, minor and trace metals during basalt weathering and groundwater transport at Mt. Etna volcano (Sicily). Geochim. Cosmochim. Acta 64, 1827–1841.

Bach, W., Klein, F., 2009. The petrology of seafloor rodingites: insights from geochemical reaction path modeling. Lithos 112, 103–117.

Barriga, F., Fyfe, W.S., 1983. Development of rodingite in basaltic rocks in serpentinites, East Liguria, Italy. Contrib. Mineral. Petrol. 84, 146–151.

Barth, M., Gluhak, T., 2009. Geochemistry and tectonic setting of mafic rocks from the Othris Ophiolite, Greece. Contributions to Mineralogy and Petrology 157, 23–40.

Beard, J.S., Hopkinson, L., 2000. A fossil, serpentinization-related hydrothermal vent, Ocean Drilling Program Leg 173, Site 1068 (Iberia Abyssal Plain): some aspects of mineral and fluid chemistry. J. Geophys. Res. 105:16527–16539. https://doi.org/10.1029/2000jb900073.

Berman, R.G., 2007. winTWQ (version 2.3): a software package for performing internally-consistent thermobarometric calculations. Geological Survey of Canada, Open File 5462, (ed. 2.32).

Bernoulli, D., Manatschal, G., Desmurs, L., Müntener, O., Dilek, Y., Newcomb, S., 2003. Where did Gustav Steinmann see the trinity? Back to the roots of an Alpine ophiolite concept, Ophiolite Concept and the Evolution of Geological Thought. Geol. Soc. Am. Spec. Pap. 373, 93–110.

Boschi, C., Bonatti, E., Ligi, M., Brunelli, D., Dallai, L., D'Orazio, M., Früh-Green, G., Tonarini, S., Barnes, J.D., Bedini, R., 2013. A 10 Ma year old window into deep hydrothermal circulation at the Vema Fracture Zone (11°N, MAR). Lithos 178, 3–23.

Bourdelle, F., Cathelineau, M., 2015. Low-temperature chlorite geothermometry: a graphical representation based on a T–R+2–Si diagram. Eur. J. Mineral. 27, 617–626.

Bourdelle, F., Parra, T., Chopin, C., Beyssac, O., 2013. A new chlorite geothermometer for diagenetic to low-grade metamorphic conditions. Contrib. Mineral. Petrol. 165, 723–735.

Buse, B., Schumacher, J., Sparks, R., Field, M., 2010. Growth of bultfonteinite and hydrogarnet in metasomatized basalt xenoliths in the B/K9 kimberlite, Damtshaa, Botswana: insights into hydrothermal metamorphism in kimberlite pipes. Contrib. Mineral. Petrol. 160, 533–550.

Capedri, S., Toscani, L., Grandi, R., Venturelli, G., Papanikolaou, D., Skarpelis, N.S., 1997. Triassic volcanic rocks of some type-localities from the Hellenides. Chem. Erde 57, 257–276.

Coleman, R.G., 1977. Ophiolites. Ancient Oceanic lithosphere? Springer, Berlin - Heidelberg- New York, pp. 1–229

Collins, N.C., Bebout, G.E., Angiboust, S., Agard, P., Scambelluri, M., Crispini, L., John, T., 2015. Subduction zone metamorphic pathway for deep carbon cycling: II. Evidence from HP/UHP metabasaltic rocks and ophicarbonates. Chem. Geol. 412, 132–150.

Cook-Kollars, J., Bebout, G.E., Collins, N.C., Angiboust, S., Agard, P., 2014. Subduction zone metamorphic pathway for deep carbon cycling: I. Evidence from HP/UHP metasedimentary rocks, Italian Alps. Chem. Geol. 386, 31–48.

Denny, A.R., Kelley, D.S., Früh-Green, G.L., 2015. Geologic evolution of the Lost City Hydrothermal Field. Geochem. Geophys. Geosyst. 17, 375–394.

Deschamps, F., Godard, M., Guillot, S., Hattori, K., 2013. Geochemistry of subduction zone serpentinites: a review. Lithos 178, 96–127.

Dijkstra, A.H., Drury, M.R., Vissers, R.L.M., 2001. Structural petrology of plagioclase peridotites in the West Othris mountains (Greece): melt impregnation in Mantle Lithosphere. J. Petrol. 42, 5–24.

Dubińska, E., 1997. Rodingites and amphibolites from the serpentinites surrounding Göry Sowie block (Lower Silesia, Poland): record of supra-subduction zone magmatism and serpentinization. N. Jb. Mineral. (Abh.) 171, 239–279.

Dubińska, E., Bylina, P., Kozłowski, A., 2004. Garnets from Lower Silesia rodingites: constraints from their chemistry – Prace Specjalne (Special Papers). PTMin 24, 135–139.

Economou, E.M., Paraskevopoulos, G.M., 1989. Platinum-group elements and gold in komatiitic rocks from the Agrilia Formation, Othrys ophiolite complex, Greece. Chem. Geol. 77, 149–158.

Ferrière, J., 1974. Etude géologique d'un secteur des zones helléniques internes subpélagonienne et pélagonienne (massif de l'Othrys-Grèce continentale). Importance et signification de la période orogénique anté-Crétacé supérieur. Bull. Soc. Géol. France 7, 543–562.

Ferrière, J., 1982. Paleogeopraphie et tectoniques superposées dans les Hellénides internes: les massifs de l'Othrys et du Pélion (Grèce septentrional). 8. Thése, sciences Univ. Lille- Societe Géologique Du Nord, pp. 1–970.

Ferrière, J., Chanier, F., Ditbanjong, P., 2012. The Hellenic ophiolites: eastward or westward obduction of the Maliac Ocean, a discussion. Int. J. Earth Sci. 101, 1559–1580.
Ferrière, J., Baumgartner, P.O., Chanier, F., 2016. The Maliac Ocean: the origin of Tethyan Hellenic ophiolites. Int. J. Earth Sci.:1–23 https://doi.org/10.1007/s00531-016-1303-6.
Fettes, D., Desmons, J., 2007. Metamorphic Rocks: A Classification and Glossary Terms. Cambridge, p. 244.
Frost, B.R., Beard, J.S., 2007. On silica activity and serpentinization. J. Petrol. 48, 1351–1368.
Fryer, P., 2002. Recent studies of serpentinite occurrences in the oceans: mantle–ocean interactions in the plate tectonic cycle. Chemie der Erde-Geochem. 62, 257–302.
Grant, J.A., 1986. The isocon diagram; a simple solution to Gresens' equation for metasomatic alteration. Econ. Geol. 81, 1976–1982.
Gresens, R.L., 1967. Composition-volume relationships of metasomatism. Chem. Geol. 2, 47–65.
Guillot, S., Schwartz, S., Reynard, B., Agard, P., Prigent, C., 2015. Tectonic significance of serpentinites. Tectonophysics 646, 1–19.
Haas, J.R., Shock, E.L., Sassani, D.C., 1995. Rare earth elements in hydrothermal systems: Estimates of standard partial molal thermodynamic properties of aqueous complexes of the rare earth elements at high pressures and temperatures. Geochim. Cosmochim. Acta 59, 4329–4350.
Inoue, A., Meunier, A., Patrier-Mas, P., Rigault, C., Beaufort, D., Vieillard, P., 2009. Application of chemical geothermometry to low-temperature trioctahedral chlorites. Clay Clay Miner. 57, 371–382.
Katsikatsos, G., 1992. Geology of Greece. University of Patras, pp. 1–451.
Kelley, K.A., Cottrell, E., 2009. Water and the oxidation state of subduction zonemagmas. Science 325, 605–607.
Kelley, S.A., Osburn, G.R., Kempter, K.A., 2007. Geology of Cañon de San Diego, southwestern Jemez Mountains, north-central New Mexico: New Mexico Geological Society, 58th Field Conference. Guidebook 157–173.
Kerrick, D.M., Connolly, J.A.D., 1998. Subduction of ophicarbonates and recycling of CO_2 and H_2O. Geology 26, 375–378.
Knauss, K.G., Dibley, M.J., Bourcier, W.L., Shaw, H.F., 2001. Ti(IV) hydrolysis constants derived from rutile solubility measurements made from 100 to 300 °C. Appl. Geochem. 16, 1115–1128.
Koutsovitis, P., 2009. Petrological and Mineralogical research of the Ophiolitic rocks in the region of Eastern Othris, Greece. PhD Thesis. University of Athens, Greece, pp. 1–535.
Koutsovitis, P., 2012. Gabbroic rocks in ophiolitic occurrences from East Othris, Greece: petrogenetic processes and geotectonic environment implications. Mineral. Petrol. 104, 249–265.
Koutsovitis, P., Magganas, A., Ntaflos, T., 2012. Rift and intra-oceanic subduction signatures in the Western Tethys during the Triassic: the case of ultramafic lavas as part of an unusual ultramafic-mafic-felsic suite in Othris, Greece. Lithos 144-145, 177–193.
Koutsovitis, P., Magganas, A., Pomonis, P., Ntaflos, T., 2013. Subduction-related rodingites from East Othris, Greece: mineral reactions and physicochemical conditions of formation. Lithos 172-173:139–157. https://doi.org/10.1016/j.lithos.2013.04.009.
Koutsovitis, P., 2017. High-pressure subduction-related serpentinites and metarodingites from East Thessaly (Greece): Implications for their metamorphic, geochemical and geodynamic evolution in the Hellenic–Dinaric ophiolite context. Lithos 276, 122–145.
Lafay, R., Deschamps, F., Schwartz, S., Guillot, S., Godard, M., Debret, B., Nicollet, C., 2013. High-pressure serpentinites, a trap-and-release system controlled by metamorphic conditions: example from the Piedmont zone of the western Alps. Chem. Geol. 343, 38–54.
Lanari, P., Wagner, T., Vidal, O., 2014. A thermodynamic model for di-trioctahedral chlorite from experimental and natural data in the system MgO–FeO–Al2O3–SiO2–H2O: applications to P–T sections and geothermometry. Contrib. Mineral. Petrol., 167, 968–xxx
Li, X.P., Rahn, M., Bucher, K., 2004. Metamorphic processes in rodingites of the Zermatt-Saas ophiolites. Int. Geol. Rev. 46, 28–51.
Li, X.P., Zhang, L., Wei, C., Ai, Y., Chen, J., 2007. Petrology of rodingite derived from eclogite in western Tianshan, China. J. Metamorph. Geol. 25, 363–382.
Li, X.P., Rahn, M., Bucher, K., 2008. Eclogite facies metarodingites – phase relations in the system SiO_2-Al_2O_3-Fe_2O_3-FeO-MgO-CaO-CO_2-H_2O: an example from the Zermatt-Saas ophiolite. J. Metamorph. Geol. 26, 347–364.
Li, X.-P., Duan, W.-Y., Zhao, L.-Q., Schertl, H.-P., Kong, F.-M., Shi, T.-Q., Zhang, X., 2017. Rodingites from the Xigaze ophiolite, southern Tibet – new insights into the processes of rodingitization. Eur. J. Mineral. 29, 821–837.
Magganas, A., 2002. Constraints on the petrogenesis of Evros ophiolite extrusives, NE Greece. Lithos 65, 165–182.
Magganas, A., Koutsovitis, P., 2015. Composition, melting and evolution of the upper mantle beneath the Jurassic Pindos Ocean inferred by Ophiolitic Ultramafic Rocks in East Othris, Greece. Int. J. Earth Sci. 104, 1185–1207.
Magganas, A., Kyriakopoulos, K., 2005. Meta-pyroclastic and meta-volcanic rocks of mid-Triassic age in western Attica. 2nd Econonic Geological & Mineralogical Conference-GSG Thessaloniki, pp. 189–198 (in Greek with English abstract).
Magganas, A., Kyriakopoulos, K., Lekkas, E., 1997. Early Alpine rift volcanism in Continental Greece: the case of Glykomilia area (Koziakas Mountains). Chem. Erde 57, 243–255.
Mcdonough, W.F., Sun, S.S., 1995. The composition of the Earth. Chem. Geol. 120, 223–253.
Monjoie, P., Lapierre, H., Tashko, A., Mascle, G.H., Dechamp, A., Muceku, B., Brunet, P., 2008. Nature and origin of the Triassic volcanism in Albania and Othrys: a key to understanding the Neotethys opening? Bulletin de la Societe Geologique de France 179, 411–425.
Morimoto, N., 1988. Nomenclature of pyroxenes. Mineral. Mag. 52, 535–550.
Normand, C., Williams-Jones, A.E., 2007. Physicochemical conditions and timing of rodingite formation: evidence from rodingite-hosted fluid inclusions in the JM Asbestos mine, Asbestos, Québec. Geochem. Trans. 8, 11.
O'Hanley, D.S., 1996. Serpentinites: records of tectonic and petrological history. Oxf. Monogr. Geol. Geophys. 34, 1–277.
O'Hanley, D.S., Schandl, E.S., Wicks, F.J., 1992. The origin of rodingites from Cassiar, British Columbia, and their use to estimate T and P(H2O) during serpentinization. Geochim. Cosmochim. Acta 56, 97–108.
Palandri, J.L., Reed, M.H., 2004. Geochemical models of metasomatism in ultramafic systems: serpentinization, rodingitization, and sea floor carbonate chimney precipitation. Geochim. Cosmochim. Acta 68, 1115–1133.
Papanikolaou, D., 2009. Timing of tectonic emplacement of the ophiolites and terrane paleogeography in the Hellenides. Lithos 108, 262–280.
Pe-Piper, G., 1998. The nature of Triassic extension-related magmatism in Greece; evidence from Nd and Pb isotope geochemistry. Geol. Mag. 135, 331–348.
Pe-Piper, G., Piper, D.J.W., 2002. The Igneous Rocks of Greece. Borntraeger, Stuttgart, pp. 1–645.
Piccoli, F., Brovarone, A.V., Beyssac, O., Martinez, I., Ague, J.J., Chaduteau, C., 2016. Carbonation by fluid–rock interactions at high-pressure conditions: implications for carbon cycling in subduction zones. Earth Planet. Sci. Lett. 445, 146–159.
Pomonis, P., Tsikouras, B., Hatzipanagiotou, K., 2007. Petrogenetic evolution of the Koziakas ophiolite complex (W. Thessaly, Greece). Mineral. Petrol. 89, 77–111.
Price, I., 1977. Deposition and derivation of clastic carbonates on a Mesozoic continental margin, Othris, Greece. Sedimentology 24, 529–546.
Price, R.C., Gray, C.M., Wilson, R.E., Frey, F.A., Taylor, S.R., 1991. The effects of weathering on rare-earth element, Y and Ba abundances in Tertiary basalts from southeastern Australia. Chem. Geol. 93, 245–265.
Rassios, A., 1990. Geology and copper mineralization of the Vrinera area, east Othris ophiolite, Greece. Ofioliti 15, 287–304.
Reimann, C., De Caritat, P., 1998. Chemical Elements in the Environment: Factsheets for the Geochemist and Environmental Scientist. Springer, Heidelberg, Germany, pp. 1–398.
Robertson, A.H.F., 2002. Overview of the genesis and emplacement of Mesozoic ophiolites in the Eastern Mediterranean Tethyan region. Lithos 65, 1–67.
Robertson, A.H.F., 2004. Development of concepts concerning the genesis and emplacement of Tethyan ophiolites in the Eastern Mediterranean and Oman regions. Earth Sci. Rev. 66, 331–387.
Robertson, A.H.F., 2007. Overview of tectonic settings related to the rifting and opening of Mesozoic ocean basins in the Eastern Tethys: Oman, Himalayas and Eastern Mediterranean regions. 282. Geological Society, London, Special Publications, pp. 325–388.
Robertson, A.H.F., Clift, P.D., Degnan, P.J., Jones, G., 1991. Palaeogeographic and palaeotectonic evolution of the Eastern Mediterranean Neotethys. Palaeogeogr. Palaeoclimatol. Palaeoecol. 87, 289–343.
Roddick, J.C., Cameron, W.E., Smith, A.G., 1979. Permo-Triassic and Jurassic ^{40}Ar-^{39}Ar ages from Greek ophiolites and associated rocks. Nature 279, 788–790.
Rowe, R.K., Rimal, S., Sangam, H.P., 2009. Ageing of HDPE geomembrane exposed to air, water and leachate at different temperatures. Geotext. Geomembr. 27 (2):131–151. https://doi.org/10.1016/j.geotexmem.2008.09.007.
Schandl, E.S., Mittwede, S.K., 2001. Evolution of the Acipayam (Denizli, Turkey) Rodingites. Int. Geol. Rev. 43, 611–623.
Schandl, E.S., O'Hanley, D.S., Wicks, F.J., 1989. Rodingites in serpentinized ultramafic rocks of the Abitibi greenstone belt. Ontario. Can. Mineral. 27, 579–591.
Schwartz, S., Guillot, S., Reynard, B., Lafay, R., Debret, B., Nicollet, C., Lanari, P., Auzende, A. L., 2013. Pressure-temperature estimates of the lizardite/antigorite transition in high pressure serpentinites. Lithos 178, 197–210.
Schwarzenbach, E.M., Früh-Green, G.L., Bernasconi, S.M., Alt, J.C., Plas, A., 2013. Serpentinization and the incorporation of carbon: a study of two ancient peridotite-hosted hydrothermal systems. Chem. Geol. 351, 115–133.
Smith, A.G., 1979. Othris, Pindos and Vourinos ophiolites and the Pelagonian zone.- Institute of Geological Mining Research, Athens, Greece. 6th Colloquium on the Geology of the Aegean Region. 3, pp. 1369–1374.
Smith, A.G., Rassios, A., 2003. The evolution of ideas for the origin and emplacement of the western Hellenic ophiolites. Geol. Soc. Am. Spec. Pap. 373, 337–350.
Smith, A.G., Hynes, A.J., Menzies, M., Nisbet, E.G., Price, I., Welland, M.J., Ferrière, J., 1975. The stratigraphy of the Othris Mountains, eastern central Greece: a deformed Mesozoic continental margin sequence. Eclogue Geologicae Helvetiae 68, 463–481.
Spray, J.G., Bébien, J., Rex, D.C., Roddick, J.C., 1984. Age constraints on the igneous and metamorphic evolution of the Hellenic-Dinaric ophiolites. Geol. Soc. Lond., Spec. Publ. 17, 619–627.
Stampfli, G., Vavassis, I., De Bono, A., Rosselet, F., Matti, B., Bellini, M., 2003. Remnants of the Paleotethys oceanic suture-zone in the western Tethyan area. Bolletino della Societa Geologica Italiano, Volume speciale 2, 1-23.
Tsikouras, B., Pe-Piper, G., Piper, D.J.W., Hatzipanagiotou, K., 2008. Triassic rift-related komatiite, picrite and basalt, Pelagonian continental margin, Greece. Lithos 104, 199–215.
Tsikouras, B., Karipi, S., Rigopoulos, I., Perraki, M., Pomonis, P., Hatzipanagiotou, K., 2009. Geochemical processes and petrogenetic evolution of rodingite dykes in the ophiolite complex of Othrys (Central Greece). Lithos 113, 540–554.
Verma, S.P., 1992. Seawater alteration effects on REE, K, Rb, Cs, Sr, U, Th, Pb and Sr-Nd-Pb isotope systematics in Mid-Ocean Ridge Basalt. Geochem. J. 26, 159–177.
Vils, F., Müntener, O., Kalt, A., Ludwig, T., 2011. Implications of the serpentine phase transition on the behaviour of beryllium and lithium-boron of subducted ultramafic rocks. Geochim. Cosmochim. Acta 75, 1249–1271.
Wood, B.J., 1991. Oxygen barometry of spinel peridotites. Oxygen barometry of spinel peridotites. In: Lindsley, D.H. (Ed.), Oxide Minerals: Petrologic and Magnetic Significance. Reviews in Mineralogy 25, pp. 417–431.